Antti Hakkarainen

Proton-decoupled *in vivo* ^{31}P magnetic resonance spectroscopy of the human liver

School of Electrical Engineering

Thesis submitted for examination for the degree of Master of Science in Technology.

Espoo 8.11.2017

Thesis supervisor:

Prof. Raimo Sepponen

Thesis instructor:

Doc. Jaana Hiltunen

Aalto University
School of Electrical Engineering

AALTO-YLIOPISTO
SÄHKÖTEKNIIKAN KORKEAKOULU

DIPLOMITYÖN
TIIVISTELMÄ

Tekijä: Antti Hakkarainen

Työn nimi: Maksan protoni-irtikytketty fosforispektroskopia kliinisellä magneettikuvauslaitteella

Päivämäärä: 8.11.2017 Kieli: Englanti Sivumäärä:8+68

Biotieteiden teknologioiden maisteriohjelma

Pääaine: Bioanturit ja Bioeletroniikka Koodi: ELEC3045

Valvoja: Prof. Raimo Sepponen

Ohjaaja: Dos. Jaana Hiltunen

In vivo magneettiresonanssi fosforispektroskopialla voidaan tutkia maksan metaboliaa kajoamattomasti ottamatta näytepalaa maksakudoksesta. Lisäämällä paikannussekvenssiin radiotaajuista säteilyä kohteeseen protonien Larmor-taajuudella ennen signaalin keruuta voidaan siirtää protonien polarisaatiota fosforiytimille ja parantaa signaalikohinasuhdetta. Säteilyttämällä vastaavasti signaalin keruun aikana on mahdollista päästä eroon protonien ja fosforiytimien välisestä kytkeytymisestä ja parantaa resonanssien erottelukykyä. Resoluutio ja signaalikohinasuhde ovat kriittisiä ominaisuuksia suhteellisen epäherkässä menetelmässä, jossa signaalit resonoivat osin päällekäin. Polarisaation siirto on kuitenkin metaboliitti- ja osin yksilökohtaista ja voi potentiaalisesti lisätä hajontaa.

Tässä diplomityössä on simuloitu maksan fosforispektrejä ja tutkittu kohinan ja resonanssipiikkien levenemisen vaikutusta kvantitointiin. Työssä mitattiin kuusi tervettä koehenkilöä. Simuloinneissa saatua tietoa on hyödynnetty, kun mittausdatasta on määritetty metaboliittikohtaiset signaalikohinasuhteet sekä yksilöiden sisäiset että väliset toistettavuudet metaboliittikonsentraatioiden määrittämiseksi. Kohinaisissa spektreissä viivamuotosovitukset toimivat hyvin. Gaussinen viivamuoto aliarvioi intensiteettejä, mutta ei ole riippuvainen piikkien puoliarvoleveyksistä. Lorentzinen viivamuoto yliarvioi intensiteettejä ja on herkkä piikkien levenemiselle ellei intensiteettejä normalisoida spektrin kokonaissignaaliin. *In vivo* spektreissä hajonta oli pienempää Lorentzisella viivamuodolla verrattuna Gaussiseen viivamuotoon. Variaatiokertoimet yksilöiden sisäiselle hajonnalle olivat Gaussisella sovituksella 7-60 % ja yksilöiden väliselle 24-67%. Lorentzisella sovituksella vastaavat variaatiokertoimet olivat välillä 2-59% ja 10-43%. Diplomityössä määritettyjä toistettavuuksia voidaan käyttää pohjana tilastollisille voima-analyyseille kliinisiä tutkimuksia suunniteltaessa.

Avainsanat: Magneettiresonanssispektroskopia, maksa, magneettikuvaus, fosforispektroskopia

AALTO UNIVERSITY
SCHOOL OF ELECTRICAL ENGINEERING

ABSTRACT OF THE
MASTER'S THESIS

Author: Antti Hakkarainen

Title: Proton-decoupled *in vivo* ^{31}P magnetic resonance spectroscopy of the human liver

Date: 8.11.2017 Language: English Number of pages:8+68

Master's Programme in Life Science Technologies

Major: Biosensing and Bioelectronics Code: ELEC3045

Supervisor: Prof. Raimo Sepponen

Instructor: Doc. Jaana Hiltunen

^{31}P magnetic resonance spectroscopy can be used to study phosphorus metabolism in the liver non-invasively. Spectral resolution and signal-to-noise ratio (SNR) are critical issues in *in vivo* ^{31}P MRS, since relevant peaks overlap partly and the NMR sensitivity of ^{31}P is only 6 % of protons sensitivity. Spectral resolution and sensitivity in ^{31}P MRS can be improved by applying a proton-decoupling and nuclear Overhauser schemes to the measurement sequence. However, nuclear overhauser enhancement is individual for each metabolite and may have inter-individual variation as well.

In this thesis, the effects of line broadening and noise on hepatic ^{31}P MR spectra were studied through simulations. In addition, hepatic *in vivo* proton-decoupled ^{31}P MRS measurement were performed on healthy subjects to determine SNR, and inter- and intra-individual variations for each metabolite. Information obtained from simulated spectra were utilized in the analysis of *in vivo* spectra.

In this thesis, lineshape fitting combined with prior knowledge was insensitive to noise. Lorentzian lineshape fit tends to overestimate broad resonances if not normalized by total phosphorus signal, while Gaussian lineshapes are insensitive to inhomogeneaous broadening, but underestimate signal intensities. Lorentzian compared to Gaussian approach resulted lower variation in *in vivo* spectra: inter- and intra-individual coefficient of variations for Gaussian fitting procedure ranged from 24-67% and 7-60%, and Lorentzian 10-43% and 2-59%, respectively. These variations can be utilized in power calculations for clinical studies.

Keywords: Nuclear magnetic resonance, 31-Phosphorus magnetic resonance spectroscopy, Liver

Esipuhe

Tämän diplomityön magneettitutkimukset tehtiin HUS-Kuvantamisen kliinisellä magneettikuvauslaitteella. Kuvaukset ovat olleet osa fosforispektroskopian kehitysprojektia, jossa vastuuhenkilönä on toiminut Dosentti Nina Lundbom. Haluan osoittaa suuret kiitokseni Ninalle kaikesta saamastani mentoroinnista. Haluan myös kiittää HUS-kuvantamisen johtoa mahdollisuudesta tehdä tutkimusta ja kollektiivisesti kaikkia projektissa mukana olleita kollaboraattoreita.

Työni valvojaa Professori Raimo Sepposta haluan kiittää saamistani nopeista kommenteista, jotta olen voinut viedä prosessia sujuvasti eteenpäin. Työni ohjaajaa Dosentti Jaana Perkolaa (ent. Hiltunen) haluan kiittää erinomaisesta ohjauksesta, mielenkiintoisista keskusteluista ja työlleni uhraamastaan ajasta. Jaanan rakentavat ehdotukset työni loppuvaiheessa ovat tehneet työstä huomattavasti selkeämmän ja havainnollisemman.

Diplomityöni kirjoittamisessa ratkaisevassa asemassa ovat olleet lapsia hoitaneet Liisa-mummu ja Heli-mummi. Työ on kirjoitettu pääosin perhevapaan aikana eikä olisi onnistunut ilman hoitoapua. Siitä kiitokset lasteni isoäideille. Kiitokset kuuluvat myös isälleni Tarvolle ja apelleni Olaville.

Lopuksi haluan kiittää kotijoukkojani kaikesta rakkaudesta ja tuesta. Kiitos Leena, Nuutti ja Eino!

Otaniemi, 8.11.2017

Antti I. Hakkarainen

Contents

Abstract (in Finnish) ii

Abstract iii

Esipuhe iv

Sisällysluettelo v

Symbols and abbreviations vii

1 Introduction 1
- 1.1 A brief history to ^{31}P magnetic resonance spectroscopy . . . 1
- 1.2 Methods to study liver metabolism . . . 2
- 1.3 Hepatic ^{31}P MRS . . . 3
- 1.4 Aim of the thesis . . . 4

2 Theory of hepatic NMR 5
- 2.1 Excitation and relaxation . . . 6
  - 2.1.1 Relaxation . . . 7
  - 2.1.2 The dynamics of T_1 and T_2 relaxations . . . 8
  - 2.1.3 Relaxation mechnisms of ^{31}P metabolites . . . 12
- 2.2 Data acquisition . . . 13
  - 2.2.1 Measurement coil . . . 13
  - 2.2.2 RF pulses . . . 15
  - 2.2.3 Spatial localization . . . 15
- 2.3 Magnetic resonance spectroscopy . . . 16
  - 2.3.1 Chemical shift . . . 17
  - 2.3.2 J-coupling . . . 18
  - 2.3.3 Proton-decoupling . . . 19
  - 2.3.4 Nuclear Overhauser effect . . . 21
- 2.4 Processing of the NMR signal . . . 21
  - 2.4.1 Zero filling . . . 21
  - 2.4.2 Time domain filtering . . . 22
  - 2.4.3 Fourier transform . . . 24
  - 2.4.4 Phase Correction . . . 25
  - 2.4.5 Quantification . . . 26
  - 2.4.6 Error estimation . . . 27
- 2.5 The liver and ^{31}P metabolites . . . 28
  - 2.5.1 Liver anatomy . . . 28
  - 2.5.2 Liver physiology . . . 30
  - 2.5.3 Phosphomonoesters . . . 31
  - 2.5.4 Phosphodiesters . . . 32
  - 2.5.5 Inorganic phosphates . . . 32
  - 2.5.6 Phosphoenolpuryvate and phosphatidylcholine . . . 33

2.5.7 Nucleoside triphosphates 34
2.5.8 Diphosphodiesters 35
2.5.9 Other metabolites and contamination from non-hepatic tissue 36

3 Experiments **37**
3.1 Simulations 37
3.2 Measurements 38
3.3 In vivo measurements 38
3.4 ^{31}P MRS acquisition 39
3.4.1 Shimming 41
3.4.2 Tuning and matching 42
3.4.3 Signal processing and quantification 43
3.5 ^{1}H MRS acquisition and signal processing 44

4 Results **48**
4.1 The effect of line broadening and noise on metabolite concentrations . 48
4.2 *In vivo* ^{31}P MRS 49
4.3 *In vivo* ^{1}H MRS 49

5 Discussion **54**
5.1 Discrepancy between simulated and *in vivo* spectra 54
5.2 Effects of imperfect localization 55
5.3 Signal contamination from non-hepatic tissues 55
5.4 Effect of physiological state and diat on metabolite levels 57
5.5 Effects related to measurement parameters 57
5.6 Field strenght considerations 58
5.7 In summary 58

Symbols and abbreviations

Symbols

$\mathbf{B}$	magnetic field
k	Boltzmann's contant $\approx 1.3805 \times 10^{-23}[J/K]$
h	Planks's contant $\approx 6.62607 \times 10^{-34}[m^2kg/s]$
γ	gyromagnetic ratio
ν_0	Larmor frequency
r	internuclear distance
η	nuclear Overhauser enhancement
ρ_L	reflection coefficient
τ_C	correlation time
M_0	net magnetization
M_z	longitudinal magnetization
M_{xy}	transverse magnetization
$T1$	longitudinal i.e. spin-lattice relaxation
$T2$	transverse i.e. spin-spin relaxation
^{31}P	phosphorus isotope with mass number of 31
^{1}H	hydrogen isotope with mass number of 1 (proton)
^{19}F	fluorine isotope with mass number of 19
^{13}C	carbon isotope with mass number of 13 (proton)

Opetators

$\frac{\mathrm{d}}{\mathrm{d}t}$	a derivative in respect to time (t)
$\frac{\partial}{\partial t}$	the partial derivative in respect to t.
$\int_{-\infty}^{\infty}$	improper integral with infinite endpoints

Abbreviations

AFP	adiabatic full passage pulse
AHP	adiabatic half passage pulse
AMARES	advanced method for accurate, robust, and efficient spectral fitting
AMP	adenosine monophosphate
ATP	adenosine triphosphate
CRB	Cramér-Rao bound
CRLB	Cramér-Rao lower bound
CSA	chemical shift anisotropy
CV	coefficient of variation
DW-MRI	diffusion weighted magnetic resonance imaging
emf	electromotive force
FID	free induction decay
GPC	glycerophosphorylcholine
GPE	glycerophosphorylethanolamine
HS	hyperbolic secant
HS-EX	hyperbolic secant excitation
ISIS	image selected in vivo spectroscopy
LWHM	line width at half maximum
MRE	magnetic resonance elastography
MRI	magnetic resonance imaging
MRS	magnetic resonance spectroscopy
NADPH	nicotinamide adenine dinucleotide phosphate
NMR	nuclear magnetic resonance
NOE	nuclear overhauser effect
NS	number of scans
NTP	nucleoside triphophate
PB	pencil beam
PDE	phosphodiesters
PC	phosphocholine
PCr	phosphocreatine
PE	phosphoethanolamine
PEP	phosphoenolpyruvate
Pi	inorganic phosphates
PME	phosphomonoesters
PtdC	phosphatidylcholine
RF	radiofrequency
RG	receiver gain
PRESS	point resolved spectroscopy
RMS	root mean square
SD	standard deviation
SNR	signal-to-noise-ratio
SR	spin rotation
STEAM	stimulated echo acquisition mode
UDPG	uridine diphosphoglucose
T2DM	type 2 diabetes mellitus
TE	echo time
TR	repetition time
WALTZ-4	wideband alternating-phase low-power technique for zero-residual splitting

1 Introduction

1.1 A brief history to ^{31}P magnetic resonance spectroscopy

Nuclear magnetic resonance (NMR) is based on magnetic properties of nuclei. Felix Bloch and Edward Mills Purcell (along with their research groups) discovered that absorption and emission of electromagnetic radiation can be observed when nuclei are placed in a strong external magnetic field [1, 2]. Bloch and Purcell were jointly awarded the Nobel Prize in physics in 1952 for their pioneering achievements.

Another giant leap towards an application of NMR spectroscopy was taken in 1950, when Proctor and Yu discovered that nuclei within the same molecule absorb energy at different resonance frequencies - a phenomena known as chemical shift [3]. In 1966, Ernst and Andersson introduced pulsed NMR in combination with Fourier transformation, which is the basis of all modern NMR experiments [4]. Ernst continued his pioneering work on methodology of NMR spectroscopy and he later had major contribution in the development of multi-dimension spectroscopy. In 1991, Ernst received the Nobel Prize in chemistry *"for his contributions to the development of the methodology of high resolution nuclear magnetic resonance (NMR) spectroscopy"*.

The first NMR experiments on biological tissue were performed in Scandinavia by a Swedish physician Erik Odeblad in mid-1950s. In Stanford in 1953, Felix Bloch had been refused Odeblad to use his NMR spectrometer and made clear that *"NMR was a tool for physicists, not for research into physiology, medicine, or biology"*. In Stockholm, Gunnar Lindström had built his own NMR instrument around 1950. After his fellow year in California, Odeblad came back to Sweden, was allowed to modify Lindström's machine and started his experiments on tissue samples [5]. Their first NMR results revealed that different tissues had distinct relaxation times and the observation was published in Acta Radiologica in 1955 [6].

In 1971, Dr. Raymond Damadian reported that NMR properties of malignand tumorous tissue differs from normal tissue, suggesting that proton NMR may have diagnostic value [7]. Although, the observation was false *per se*, it was extremely important to the development of MRI, since it got attention from financiers. Less than two years later he filed his idea for using magnetic resonance imaging as a tool for medical diagnosis with the U.S. Patent Office, entitled *"Apparatus and Method for Detecting Cancer in Tissue."* A U.S. patent was granted in February 1974 [8] and it was the world's first patent issued in the field of MRI. By 1977, Dr. Damadian completed construction of the first whole-body MRI scanner and the FONAR Corporation company he formed in 1978 produced the first commercial scanner in 1980.

Nearly 20 years after Odeblad described NMR-properties of biologic tissue, Lauterbur and Mansfield described a major application of modern *in vivo* NMR imaging or later known as magnetic resonance imaging (MRI)[9, 10, 11]. They were able to reconstruct the spatial distribution of the spins in form of an image by applying position dependent magnetic fields in addition to static magnetic field. In 2003, Lauterbur and Mansfield were jointly awarded the Nobel Prize in physiology and

medicine *"for their discoveries concerning magnetic resonance imaging"*.

The first experiments of the ^{31}P NMR spectroscopy on intact living tissues were reported on early 1970s: Moon and Richard showed how intracellular pH of intact red blood cells can be determined from chemical shift differences [12] and in 1974, Hault *et al.* reported their NMR experiments on intact, excised rat hind leg [13].

Until the beginning of 1980s, all ^{31}P NMR spectroscopy studies, with probably only one exception [14], were carried out on excised, perfused organs and tissues obtained through a process requiring some form of invasive surgery. In 1980, first *in vivo* ^{31}P MRS studies on small animals were published. Spatial localization was performed using surface coils and utilizing static-field gradients [15, 16]. Animal studies were followed by first *in vivo* studies on human liver in mid-1980s [17, 18] and by the end of the decade, broadband decoupling had already been utilized in hepatic ^{31}P MRS at 1.5 T [19].

Higher field strengths are appealing for MRS experiments of the nuclei with lower concentrations or lower MR sensitivity compared to proton (^{1}H), including ^{31}P. Since 3.0 Tesla become mainstream field strength in clinical use from the mid 2000s, in practise, almost all clinical imagers are either 1.5 Tesla or 3.0 Tesla machines. Recently, first commercial 7.0 Tesla imagers have become available for clinical use, but installations are still rare.

Nowadays, *in vivo* NMR spectroscopy is widely used to study brain, liver and muscle metabolism, and it has several clinical applications. However, it is relatively time consuming and requires expertised personnel. Therefore, the role of *in vivo* MRS in clinical diagnostics remains marginal.

1.2 Methods to study liver metabolism

Liver is vital and unique organ with dual blood supply. Liver is connected to hepatic artery and the portal vein. Former carries oxygen-rich blood from the aorta and the latter nutrient-rich blood from the gastrointestinal tract. Liver has numerous functions such as maintenance of blood glucose levels and clearing harmful substances from the blood, and is thus interesting target for research. Moreover, several liver disease have malign and progressive nature, and need to be diagnosed at early stage in order to obtain successful treatment.

Currently liver biopsy remains as a golden standard for diagnosing inflammation and fibrosis in the liver, but it's also sensitive for bleeding due to vascular structure and strong blood supply of the liver. Liver biopsy has been reported to cause pain for some patients and it requires postoperative surveillance in the hospital. Even a small, but existing mortality has been reported to be involved with liver biopsy [20]. For ethical reasons, it's not allowed to take liver tissue samples from healthy subjects and therefore liver biopsy is unsuitable for a great number of academic studies. Liver biopsy has another major limitation: biopsy samples represent only approximately 1/50000 of the total liver volume. Therefore, sampling errors are frequent [21, 22].

Due to these complication risks and sampling errors, there is need for non-invasive approaches in basic research as well as in clinical diagnostics. The human

liver is attractive target for magnetic resonance spectroscopy studies: it's metabolically active and relatively homogeneous organ. Relatively large volume and superficial location allow generous acquisition volumes and proximal placement of a surface coil, respectively.

1.3 Hepatic ^{31}P MRS

Proton (^{1}H) MR spectroscopy is a well-established method used to quantify liver fat [23]. (^{13}C) MR spectroscopy has been used to quantitate glycogen storage in the liver and (^{19}F) MRS to monitor the metabolism of fluorinated drugs in the human liver [24, 25]. Moreover, ^{31}P is a very attractive isotope for liver NMR spectroscopy, since ^{31}P has a natural abundance of almost 100 % (Table 1) and it's concentrated in a relatively small variety of moieties. NMR visible phosphorus signals in the liver includes resonances arising most prominantly from phosphomonoesters (PME), phosphodiesters (PDE), inorganic phosphates (Pi), diphosphodiesters and nucleosine triphosphates.

Several diffuse liver diseases are characterized by the presence of inflammatory and fibrotic components. Fibrosis has been shown to be associated with restricted diffusion of water, diffusion-weighted magnetic resonance imaging (DW-MRI) [26]. However, DW-MRI is sensitive to liver fat and iron [27], and there is incongruity between studies. For example, Boulanger et al. were unable to demonstrate this relationship on patients with virus C hepatitis [28]. By assessing mechanical properties of the tissue transient or ultrasound and magnetic resonance elastography (MRE) can detect fibrosis [29, 30]. Several studies have reported correlation between phosphomonoester (PME) resonance (or PME/phosphodiester -ratio) and severity of liver fibrosis, measured by in vivo ^{31}P MRS and hislogy analysis, respectively [31, 32]. Recently, it has been suggested that ^{31}P MRS is more sensitive to detect inflammation or ongoing fibrogenesis rathar than the presence of fibrosis itself [33]. When these MR based methods have been compared, MRE has been shown to outperform both DW-MRI and ^{31}P MRS in detecting fibrosis [26, 34]. However, in the presence of inflammatory activity in the liver, MRE can overestimate fibrosis, and the effect of these two separate components cannot be distinquished [30].

In addition to monitoring the degree of liver damage, ^{31}P MRS can provide information about the functional status of the liver. Moreover, reduced ATP levels have been found to be associated with obesity [35, 36], type 2 diabetes mellitus (T2DM) [37] and cirrhosis [38]. Since Pi and exchange in dynamic balance, ^{31}P magnetization transfer experiment allows assessment of hepatic adenosine triphosphate (ATP) synthesis [39]. ATP synthesis has been found to be related to insulin resistance and reduced in patients with T2DM [40].

Even though, promising results have been reported from both hepatic *in vitro* and *in vivo* ^{31}P MRS studies, clinical applications are rare. Several economical and technical reasons have kept *in vivo* ^{31}P MRS in the marginal. Restricted signal-to-noise ratio and spectral resolution cause reliability and repeatability issues, while necessary dedicated hardware including separate RF-amplifier and measurement coil will be a marked extra cost.

1.4 Aim of the thesis

The aim of this thesis was to evaluate the feasibility of the hepatic in vivo ^{31}P MRS in clinical environment with the equipment available in hospital district of Helsinki and Uusimaa (HUS), and to provide recommendations for quantification strategy through analysis of simulated spectra.

In vivo measurements were restricted to single voxel spectroscopy on healthy subjects only. Absolute quantification with external concentration reference was not performed. Instead, total phosphorus signal was used as an internal reference in quantification. As a novel approach in clinical environment, nuclear Overhauser enhancement was applied to boost signal-to-noise ratio (SNR) and proton-decoupling to improve spectral resolution. Other measurement parameters were chosen to keep measurement time clinically feasible. ^{1}H MRS was performed to exclude possible fatty liver.

2 Theory of hepatic NMR

In this section, the basics of nuclear magnetic resonance is presented to the extent required for understanding the present thesis. Unless otherwise denoted, the text is based on the books of Levitt [41], Tofts [42] and de Graaf [43].

Each atomic nucleus has a physical property called spin, which, however, has almost no effect on the normal chemical and physical behaviour of substance. The only requirement for a nucleus to give an NMR absorption is that the nucleus posses a magnetic moment. Nucleus with spin quantum number I has 2I + 1 energy states. Thus, nucleus with $I \neq 0$ has more than one energy states and is NMR active. Rules of nuclear spins can be summarized in terms of the mass number A and the atomic number Z as follows:

1. The nuclear spin is half-integer if the mass number A is odd.

2. The nuclear spin is integer if the mass number A is even and the atomic number Z is odd.

3. The nuclear spin is zero if both the mass number and A and the atomic number Z are even.

Nuclei with spin $I = 1/2$ are spherical in shape, have two spin energy states and have convenient magnetic properties. Isotopes ^{1}H, ^{13}C and ^{31}P are by far the three most used isotopes in *in vivo* MRS. All of them have $I = \frac{1}{2}$, all are relatively sensitive to NMR and, of course, biologically relevant. Also, nuclei with integer spin like ^{1}H (deuterium) and ^{14}N have applications in the field NMR spectroscopy. Properties of some of the most important NMR active nuclei are shown in Table 1.

Spin states of the nucleus are quantified, and energy difference (ΔE) between the states is proportional to the strength of the external magnetic field B_0

$$\Delta E = hf = \frac{h\gamma B_0}{2\pi} \tag{1}$$

where h is Planck's constant, γ is gyromagnetic ratio and f frequency. Each nuclear spin possess a magnetic moment which is associated with the angular momentum of the nucleus. In an external magnetic field, magnetic moment starts to precess about the magnetic field direction with a frequency proportional to B_0:

$$\nu_0 = \frac{\gamma}{2\pi} B_0. \tag{2}$$

This frequency ν_0 is called Larmor-frequency and γ is a constant known as gyromagnetic ratio characteristic to each nucleus (Table 1).

In an external magnetic field (B_0), spins will align parallel (α) or antiparallel (β) to the B_0. The parallel state has lower energy and is slightly more populated compared to antiparallel state. The difference between the two populations ($I = 1/2$), α and β, is related to the energy difference by the Boltzmann distribution

$$N_\alpha / N_\beta = e^{\Delta E / kT}, \tag{3}$$

where k is Boltzmann's constant ($1.3805 \times 10^{-23} J/K$), and T is temperature in Kelvin. N_α and N_β are spin populations with parallel and antiparallel alignments, respectively. According to Equation 3 the difference between high and low energy populations is only 13 out of ten million ^{31}P nuclei at body temperature at 3.0 Tesla. This population difference produce a longitudinal net magnetization (M_0) along the main magnetic field B_0. A transition from low-energy to high-energy state must be delivered in packets of ΔE transmitted at Larmor-frequency according to Equation 1. Figure 3 shows an example of energy level diagram for a dipolar coupled two spin system with zero, single and double quantum transitions.

Table 1: Properties of the selected NMR-active isotopes with non-zero spin number I. Relative sensitivity to ^1H is proportional to the natural abundance and the cube of the gyromagnetic ratio γ. Values in in the table taken from [44].

Isotope	I	Gyromagnetic ratio γ (MHz T^{-1})	Natural Abundance (%)	Relative Sensitivity
^{1}H	$\frac{1}{2}$	42.58	99.985	1.00
^{2}H	1	6.54	0.015	0.00000145
^{7}Li	$\frac{3}{2}$	16.55	92.58	0.27123
^{13}C	$\frac{1}{2}$	10.70	1.1	0.00018
^{14}N	1	3.07	99.63	0.001
^{15}N	$\frac{1}{2}$	4.31	0.37	0.000004
^{17}O	$\frac{5}{2}$	5.77	0.037	0.00001
^{19}F	$\frac{1}{2}$	40.06	100.00	0.833
^{23}Na	$\frac{3}{2}$	11.26	100.00	0.0925
^{31}P	$\frac{1}{2}$	17.24	75.53	0.066
^{207}Pb	$\frac{1}{2}$	8.91	22.6	0.002

2.1 Excitation and relaxation

At thermal equilibrium, longitudinal magnetization is a static vector and spins have no phase coherence in the transverse plane. However, to observe NMR signal, the longitudinal magnetization is tilted towards or into the transverse plane using a second magnetic field B_1, which oscillates in the RF (MHz) range. These RF pulses applied at Larmor frequency ν_0 excite the spins. Transverse magnetization (M_{xy}) rotates about B_0 at the Larmor frequency and induces an electromotive force (emf) in the receiver coil. The amplitude of the induced emf is determined by Faraday's law of induction. This induced emf can be amplified and detected as an NMR

signal. This exponentially decaying time-domain NMR signal oscillating at Larmor frequency is known as free induction decay (FID).

2.1.1 Relaxation

Relaxation is the process by which the thermal equilibrium of the spin system is regained after RF excitation: spin populations return to state determined by the Equation 3 (T_1) and phase coherence in the transverse plane is lost (T_2). At thermal equilibrium, in the absence of time-varying magnetic fields B_1, longitudinal z component of the magnetization M is constant:

$$\frac{dM_z}{dt} = 0 \tag{4}$$

Both x and y components of **M** are zero and no NMR signal can be detected. Under the influence of B_0 and B_1, orthogonal x, y and z components of M can be described by using the complete Bloch equations [1]:

$$\frac{dM_x}{dt} = \gamma \left[M_y(t)B_0 - M_z(t)B_{1y}\right] - \frac{M_x(t)}{T_2} \tag{5}$$

$$\frac{dM_y}{dt} = \gamma \left[M_z(t)B_{1x} - M_x(t)B_0\right] - \frac{M_y(t)}{T_2} \tag{6}$$

$$\frac{dM_z}{dt} = \gamma \left[M_x(t)B_{1y} - M_y(t)B_{1x}\right] - \frac{M_z(t) - M_0}{T_1} \tag{7}$$

T_1 Relaxation

T_1 relaxation, also known as spin-lattice relaxation, characterizes the rate at which the longitudinal M_z component of the magnetization vector exponentially recovers towards its thermodynamic equilibrium (Figure 1):

$$M_z(t) = M_0(1 - e^{-t/T_1}), \tag{8}$$

The recovery is caused by the fluctuating magnetic fields arising mainly from the motion of the molecules in the neighbourhood of the magnetic moments. Therefore, the T_1 recovery rate is an indicator of the mobility of the molecules.

T_2 Relaxation

After perturbation of the magnetic field into the transverse plane, individual isochromats lose phase coherence and the net component of magnetization lying in the transverse plane dephases, and the detectable signal diminishes. T_2- or spin-spin relaxation characterizes the rate at which the transverse component of the net magnetization M_0 exponentially decays towards zero (Figure 2, left):

$$M_{xy}(t) = M_{xy}(0)e^{-t/T_2}, \tag{9}$$

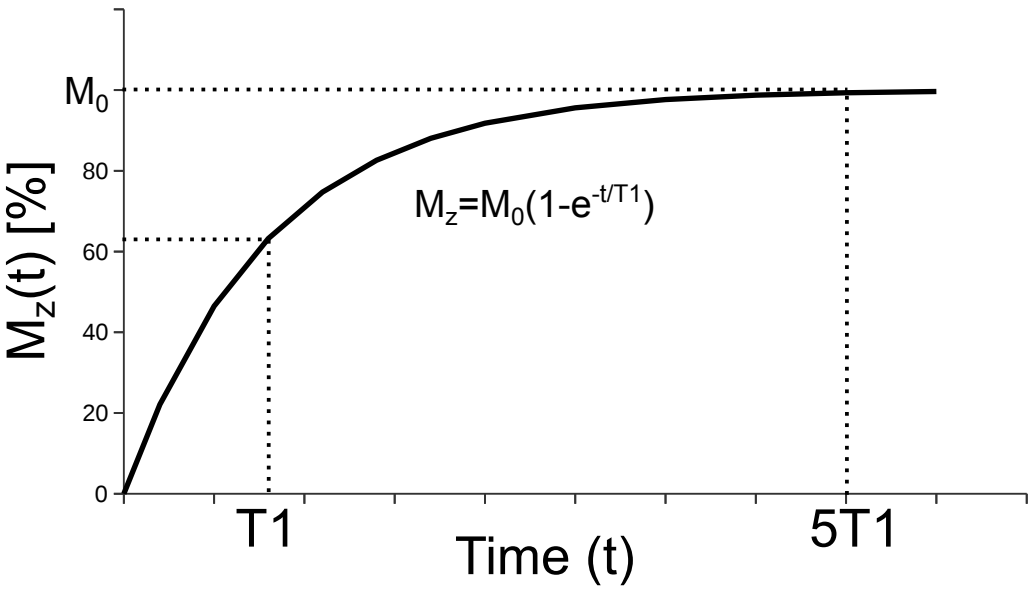

Figure 1: Exponential T_1 recovery of longitudinal magnetization M_z. In practice, magnetization is considered to be fully relaxed when t $\geq 5\times T_1$.

Local inhomogeneities within the sample make isochromats to precess slightly faster or lower. These spatial differences in precession frequencies results spins with different locations losing their phase coherence and the FID decaying faster than if the sample were in the homogeneous field. An inhomogeneous B_0 introduces additional dephasing (R'), on top of the natural T_2 decay caused by the random thermal activity of the sample. The time constant for such decay of the FID is known as T_2^*

$$\frac{1}{T_2^*} = \frac{1}{T_2} + R', \tag{10}$$

where R' ($= 1/T_2^{'}$) is an additional relaxation rate term [45].

2.1.2 The dynamics of T_1 and T_2 relaxations

Relaxation is a complex process involving several competing mechanisms. In principle, any molecular interactions which cause additional magnetic fields can affect relaxation. There are at least five different mechanisms involving the relaxation process: i) magnetic dipole-dipole interactions, ii) electric quadrupole interactions, iii) chemical shift anisotropy, iv) spin rotation interactions, v) scalar coupling interactions. Of these, dipole-dipole interactions and chemical shift anisotropy are the most relevant in this thesis, and are therefore described more in detail.

Bloembergen-Purcell-Pound (BPP) first described the theory of dipole-dipole relaxations in 1948 [2]. Dipole-dipole relaxations is normally the dominant relaxation pathway for spin 1/2 nuclei in solution.

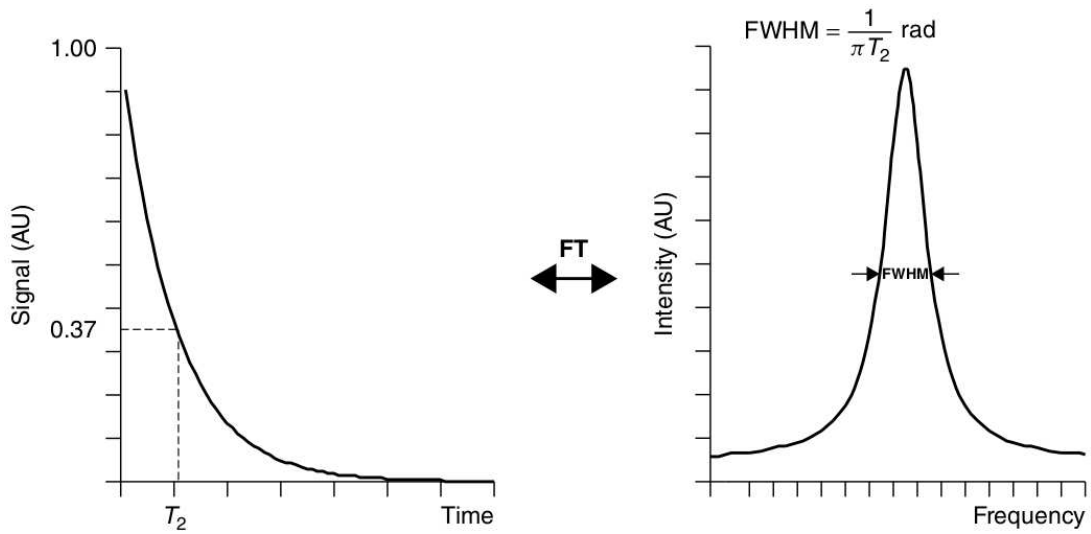

Figure 2: Monoexponential T_2 decay of signal in time domain on the left. In frequency domain (right), spectral line widths are inversely proportional to the T_2 constant. Figure is taken from [45].

Dipole-dipole interactions: The most important source of fluctuating magnetic fields are dipole-dipole interactions. where the magnetic moment of one nucleus affects to local field of neighbour nuclei in a random manner, due to molecular tumbling and Brownian motion. The relaxation itself is induced by the frequency components close to Larmor frequency (exhibited by the fluctuating magnetic fields).

In order to extract the frequency components of the local magnetic field by Fourier transform, the concept of correlations function $G(\tau)$ is introduced. The correlation function is a measure for the correlation between the local magnetic fields as time progresses. After longer τ delays the local magnetic field B_{loc} is drastically altered due to molecular tumbling and Brownian motion, whereas for short τ the local magnetic field B_{loc} will have not changed much. Correlation function is usually taken as a decaying exponential:

$$G(\tau) = \overline{B_{loc}(\tau)B_{loc}(t+\tau)} = \overline{B_{loc}^2}e^{-|\tau|/\tau_c}, \tag{11}$$

where τ_C is the correlation time, which roughly corresponds to the average time for a molecule to rotate over 1 rad. For mobile spins in the solution τ_c is short, while for immobile spins τ_c is several orders of magnitude longer.

The frequency components in the time-domain function can analyzed by Fourier transformation:

$$J(\omega) = \int_{-\infty}^{\infty} G(\tau)e^{-i\omega\tau}d\tau = 2\overline{B_{loc}^2}\frac{\tau_c}{1+\omega^2\tau_c^2} \tag{12}$$

Resulting function $J(\omega)$ in a Lorentzian form, is called the spectral density function. $\omega^2\tau_c^2 \ll 1$ represents very fast rotational motion (high frequency components), $\omega^2\tau_c^2 \approx 1$ intermediate rotational motion and $\omega^2\tau_c^2 \gg 1$ slow rotational motion (low

frequency components). Fast and slow rotational motion emphasize the high and low frequency components, respectively.

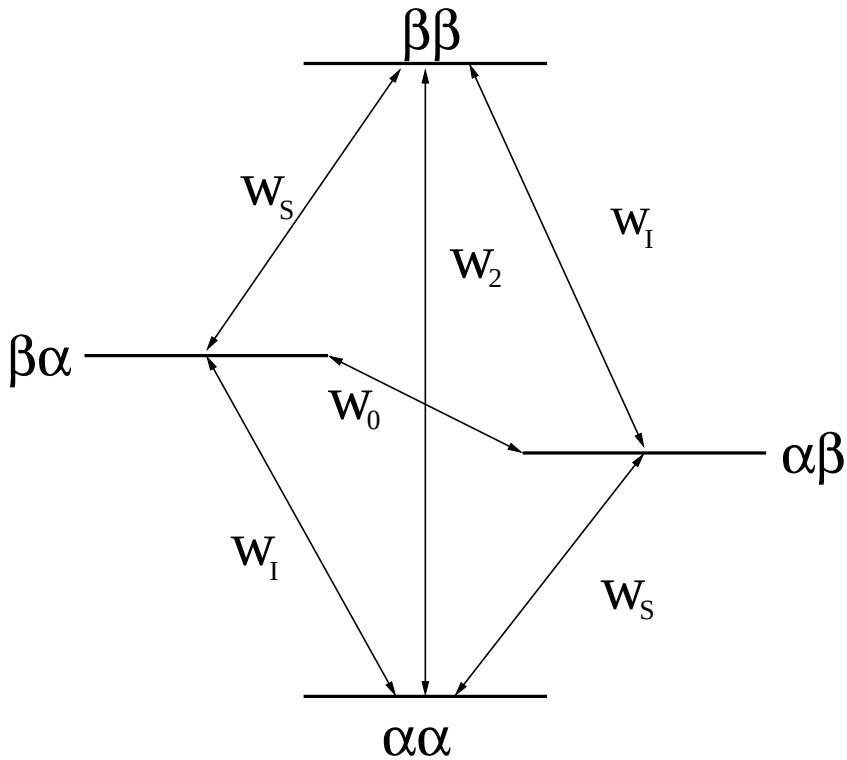

Figure 3: Energy level diagram for a dipolar coupled two spin system. W_I and W_S are probabilities for single quantum transitions of spins I and S, respectively. W_0 and W_2 are probabilities for zero and double quantum transitions, respectively.

During relaxation processes, the rate at which the occupancy of the energy levels change with time. Energy level diagram for dipolar coupled two spin system is shown in Figure 3. Spins are flagged with letters I and S. W_I, W_S represent transition probabilities that spin I or S changes energy level, respectively. W_0 and W_2 correspond to the probability of a zero or double quantum transition. The longitudinal magnetization for each spin is proportional to the difference in population across the relevant transitions. According to Solomon equations, time dependency for spins I and S is given:

$$\frac{dI_z}{dt} = -(W_0 + 2W_I + W_2)(I_Z - I_0) - (W_2 - W_0)(S_Z - S_0) \tag{13}$$

$$\frac{dS_z}{dt} = -(W_0 + 2W_S + W_2)(S_Z - S_0) - (W_2 - W_0)(I_Z - I_0), \tag{14}$$

where I_0 and S_0 are the Bolzmann equilibrium magnetizations for spins I and S. The term $(W_0 + 2W_{I,S} + W_2)$ represents the direct relaxation, while the term $(W_2 - W_0)$ represents cross relaxation between the spins. The longitudinal relaxation

is linear combination of two exponentials, caused by direct and cross relaxations. For two indentical spins with $\omega_I = \omega_S$ the recovery of longitudinal ralaxation is a single exponential and can be simplyfied to

$$\frac{d(I_z + S_z)}{dt} = -2(W_I + W_2)[(I_Z + S_Z) - (I_0 + S_0)] \tag{15}$$

The relation between transition probabilities and the relaxation rate constant can be found from the classical Bloch equation 8 and the equation 15 as follows:

$$\frac{1}{T_1} = 2W_I + 2W_2 \tag{16}$$

Analytical expression for dipolar longitudinal relaxation was first introduced by Ionel Solomon in 1955 [46]:

$$\frac{1}{T_1} = \frac{3}{10}\frac{\gamma^4 h^2}{4\pi^2 r^6}\left(\frac{\tau_c}{1+\omega^2\tau_c^2} + \frac{4\tau_c}{1+4\omega^2\tau_c^2}\right), \tag{17}$$

where r is inter-nuclear distance over which dipolar interactions take place. Corresponding expression for the transverse relaxation rate constant is given by [46]:

$$\frac{1}{T_2} = \frac{3}{20}\frac{\gamma^4 h^2}{4\pi^2 r^6}\left(3\tau_c + \frac{5\tau_c}{1+\omega^2\tau_c^2} + \frac{2\tau_c}{1+4\omega^2\tau_c^2}\right), \tag{18}$$

From the equations 17 and 18 can be seen that the T_2 relaxation is also affected by low frequency components, which dominate the relaxation in precence of slow molecular motion. The T_1 relaxation is not affected by low frequency fluctuations. If rotational motion is very fast ($\omega^2\tau_c^2 \ll 1$), T_2 equals T_1 since:

$$\frac{1}{T_1} = \frac{1}{T_2} = \frac{3}{2}\frac{\gamma^4 h^2}{4\pi^2 r^6}\tau_c \tag{19}$$

This situation ($\omega^2\tau_c^2 \ll 1$) is called *extreme narrowing limit*.

Chemical shift anisotropy (CSA): Later in the thesis, chemical shift will be presented as a single number. However, more accurate way to representation of the shielding constant is a 3×3 chemical shift tensor, because a chemical shift of the nucleus depends upon the orientation of the molecule relative to the main magnetic field direction. The relaxation rate due to chemical shift anisotrophy in the extreme narrowing limit is given by:

$$\frac{1}{T_1} = \frac{7}{45}\gamma^2 B_0^2(\sigma_\parallel - \sigma_\perp)^2\tau_c \tag{20}$$

$$\frac{1}{T_2} = \frac{2}{15}\gamma^2 B_0^2(\sigma_\parallel - \sigma_\perp)^2\tau_c, \tag{21}$$

where $\sigma_\parallel$ and $\sigma_\perp$ refer to shielding parallel and perpendicular to the symmetry axis of axial symmetry. From these equations can be seen that, in contrast to dipole-dipole relaxation, T_1 and T_2 do not equal under extreme narrowing conditions and relaxation rates (through chemical shift anisotropy) are proportional to the

square of the main magnetic field. Due to the latter, the chemical shift anisotropy becomes increasingly important relaxation mechanism as the magnetic field strength B_0 increases.

Electric quadropole moment: ^{31}P, ^{1}H and the other nuclei with spin $I = 1/2$ have a spherical charge distribution and thus they do not possess the electric quadrupole moment. The quadrupolar interaction does not contribute to relaxation when the quadrupole coupling constant is zero due to molecular symmetry. However, if the electric quadrupole moment exists for nuclei (for instance ^{23}Na), it usually dominates the relaxation process.

Spin rotation (SR) relaxation is most significant for small, symmetric molecules with short correlation times. Relaxation arises from interruption of coherent rotational motion of entire molecule. Motion generates magnetic fields, which can couple with the nuclear spin. This mechanism has only little effect, for most molecules observed with *in vivo* NMR.

Scalar relaxation is most commonly observed with quadrupole nucleus ($I > 1/2$) having short relaxation times. Usually scalar coupling has a pronounced effect on T_2 relaxation, leading for instance to line broadening in the spectrum of a spin-1/2 nuclei coupled to a quadrupolar nuclei.

2.1.3 Relaxation mechnisms of ^{31}P metabolites

Principal mechanisms for ^{31}P relaxation *in vivo* are: dipolar, intramolecular and intermolecular, chemical shift anisotropy, spin rotation, paramagnetic and scalar[47]. Of these, dipolar relaxation and chemical shift anisotrophy described above are the two major ralaxation mechanisms for ^{31}P MRS [48].

Specific experiments on model solutions indicate that chemical shift anisotropy (CSA) is the dominant mechanism for relaxation of ^{31}P nuclei in ATP at high magnetic fields, whereas dipolar interactions dominate the T_1 relaxation rate at lower fields. The reduced T_1 relaxation times for ^{31}P NMR at higher field strengths allow shorter acquisition times or improved SNR per unit of time. However, from the Equation 21 and Figure 2 we can conclude that if chemical shift anisotrophy is a dominant mechanism, the line widths increase linearly with B_0^2, whereas the frequency range increases according to B_0. Therefore, spectral resolution cannot be infinitely increased by increasing the main magnetic field, and the best resolution is not obtained at the highest magnetic field.

Dipolar relaxation is always present, CSA is present for nuclei in less than tetrahedral symmetry, and SR is likely to be significant for smaller molecules. Paramagnetic contributions are due to dissolved oxygen and other paramagnetic species. Scalar contribution is present, when couplings are modulated by exchange or a fast relaxing partner.

According to several experimental in vivo NMR studies, the transverse relaxation rate of ATP is significantly higher than that of other phosphorus containing metabolites [48]. It is unlike that this large difference is solely based on dipole-dipole interactions and chemical shift anisotrophy. It has been suggested that short transverse relaxation time of ATP is partly due to exchange between free and bound

states of ATP. The strong dipole-dipole interactions between ATP and the unpaired electron of complexed paramagnetic ion like Mn^{2+} may also decrease the transverse relaxation time.

To investigate direct contributions of different ^{31}P relaxation mechanisms *In vivo* is challenging. More practical approach is to study metabolites in pure aqueous solutions in different temperatures at different field strengths. Contributions of intra and intermolecular dipolar interactions, CSA and SR can be studied monitoring the T_1 as a function of metabolite concentration, B_0 field strength and temperature, respectively.

In a study [47], with aqueous solution Pi showed no field dependence indicating the absence of CSA contribution, which is expected for tetrahedrally symmetric ions (Figure 16). For ATP-resonances CSA-contributions are significantly smaller for the end groups (γ-phosphate), because the shielding anisotropy is less or τ_c is less due to the less restricted motion. Andrew and Gaspar measured CSA contributions of 5% and 34% for $\gamma-$ATP at 2.3 Tesla and 7.0 Tesla, respectively, whereas CSA contributions were significantly higher for $\alpha-$ATP (14% and 59%) and for $\beta-$ATP (19% and 68%) [47]. Locations phosphates γ, α and β can be seen in in structural formula in Figure 17.

In an experimental animal study the PDE resonance showed a strong field dependency in relation to other phosphorus metabolites, suggesting dominant contribution to relaxation via CSA [49]

T_1 was found to be independent of concentration in the range of 0.01−0.1 mol, suggesting that the dipolar relaxation contributions were mainly intramolecular. Typically T_1 values reported *in vivo* [50, 39] are shorter than values reported for pure aqueous solutions. This is probably due to small concentrations of paramagnetic ions, dissolved oxygen and from the presence of large molecules to which the metabolites become attached for variable residence times [47].

2.2 Data acquisition

2.2.1 Measurement coil

Radiofrequency coils are needed to rotate the longitudinal magnetization to the transverse plane and to detect the signal induced by the oscillating magnetic field B_1 in the sample. An RF coil can be seen as a LCR circuit, where L is a pure inductance of the coil and R is a resistance of the wires. The circuit is powered by the driving electromotive force (emf).

In general, the impedance Z is written in complex notation as Z = R + iX, where R is resistance and X reactance. According to the Ohm's law U=ZI, the current in the coil is inversely proportional to the impedance and thus, in practice, the impedance is minimised by eliminating the reactive component X with a parallel capasitor:

$$\omega L - \frac{1}{\omega C} = 0 \Longleftrightarrow \omega = \omega_0 = \frac{1}{\sqrt{LC}}, \tag{22}$$

where ω_0 is the natural frequency of the circuit, ω the applied emf frequency and C capasitance. RF coil is brought into resonance by adjusting the capasitor C according to equation 22. This process is usually referred as 'tuning'.

Coil is connected to preamplifier and the rest of the receiver system through standard coaxial cables with 50 Ω impedance. If the impedance of the RF coil and the sample differ from 50 Ω, which is usually the case, some of the power will be reflected according to equation[51]:

$$\rho_L = \frac{Z_L - Z_0}{Z_L + Z_0}, \tag{23}$$

where ρ_L is the reflection coefficient, Z_L is the impedance towards load and Z_0 is the impedance toward the source. If Z_L equals Z_0, the ρ_L becomes zero and no power will be lost due to reflection. To avoid signal losses, RF coil has to be also matched to 50 Ω in addition to tuning. At a certain off-resonance frequency $\omega_{50\Omega}$ the resistance equals 50 Ω plus reactance. This reactance can be nulled with a second 'matching' capasitor ´C. After introduction of ´C, the tuning capasitor has to be readjusted to make $\omega_{50\Omega}$ the Larmor frequency. Besides 'C, the RF coil is also possible to match inductively with a separe indutance coil. Tuning and matching has to be performed for each load individually.

Electric and magnetic interactions exists between the the subject and the RF coil. These subject-coil interactions are responsible for energy exchange during RF-pulse transmission and signal reception, and can be studied by quality factor Q. For the unloaded, tuned and matched RF coil the quality factor Q is:

$$Q_{unloaded} = \frac{\omega L}{R_c}, \tag{24}$$

where R_c is the resistance of the RF coil. For magnetically lossy sample such as physiological salt solution with the conductivity $\sigma \neq 0$, Q value reduces to:

$$Q_{loaded} = \frac{\omega L}{(R_c + R_m)}, \tag{25}$$

where R_m represents the effective resistance to the magnetically induced currents within the sample. The coil sensitivity is proportional to the $\sqrt{Q_{loaded}}$, thus maximisation of this value is desirable

There is not a general single coil optimal for all applications. A volume coil provides a homogenous radiofrequency field (B_1 field), resulting in uniform spin excitation across the sample. However, due to large size and poor filling factor, the sensitivity of volume coil is often compromised. For surface coils the situation is opposite: they are very sensitive, but the B_1 field is extremely inhomogenous. Thus, surface coils are desirable for signal reception and volume coils for signal transmission. In a cost effective clinical environment RF coils for nuclei other ^{1}H are often single transceiver surface coils combined with adiabatic RF pulses.

In 2010 at the 96th annual meeting of the Radiological Society of North America (RSNA) in Chicago the first commercially available digital broadband MRI system was publicly introduced. In this new Philips Ingenia MR system, radiofrequency

signals are digitized by microelectronics directly in the coil, rather than first transmitted in analog mode through coaxial cables and digitized in a converter.

2.2.2 RF pulses

RF pulses are required for all Fourier transform magnetic resonance imaging (MRI) and spectroscopy (MRS) experiments. RF pulses are essential for excitation and inversion as well as primary tool for refocusing of spin populations in MRS. Short, intense, constant-amplitude pulses are most often used to achieve uniform excitation of the spins. In a most simple case, when off-resonance effects can be neglected the nutation angle θ achieved by a RF pulse can be expressed as

$$\theta = \gamma B_1 T, \tag{26}$$

where T is the pulse lenght.

However, if the width of spectra is comparable to the applied RF field, the off-resonence effects cannot be ignored and the magnetization rotates about tilted effective field B_e. The effective magnetic field $B_[e](t)$ can be written as

$$B_e = |\mathbf{B_e}| = \sqrt{B_1^2 + \left(\frac{\Delta\Omega}{\gamma}\right)^2}, \tag{27}$$

where $\Delta\Omega$ is frequency offset. Therefore, B_1 should be replaced by B_e in the Equation 26 in the presence of off-resonance effects.

Many *in vivo* NMR experiment require more sophisticated RF pulses. B_1 magnetic field, generated by surface coils, is extremely inhomogenous and RF amplitude can vary by a factor of 10 over the sensitive volume, when using conventional RF pulses. This problem is often solved by using so called adiabatic pulses. In principal, adiabatic pulses are composed of hundreds of closely spaced hard RF pulses with different amplitude and phase. The overall effect of adibatic pulse is identical to a single hard pulse, except that adiabatic pulses generate a uniform nutation angle independent of RF amplitude above a certain threshold value.

In general, adiabatic pulses are referred as amplitude- and frequency-modulated pulses, but the latter can also be replaced by phase-modulation. Same amplitude- and frequency-modulations functions can be used for adibatic half (AHP) and full (AFP) passage pulses. AHP and AFP are used for signal excitation and inversion, respectively.

2.2.3 Spatial localization

In order to acquire the spectrum from the volume of interest, a suitable localization method is needed. Point resolved spectroscopy (PRESS) [52, 53], stimulated echo acquisition mode (STEAM) [54] and image selected in vivo spectroscopy (ISIS) [55] are the three most common, commercially availabe, volume selection methods [56]. Echo-based PRESS and STEAM dominate proton MRS, while FID-based ISIS is the most common technique for *in vivo* ^{31}P MRS due to short T_2 relaxation time of ^{31}P metabolites.

Figure 4 shows the pulse sequence diagram of ISIS sequence. The basic ISIS sequence employs three frequency-selective inversion pulses in the presence of three orthogonal magnetic fields G_x, G_y, G_z. Magnetization in a slice defined by the gradient and 180° pulse is inverted. Following the 90° excitation pulse this magnetization is 180° out-of-phase relative to the magnetization elsewhere in the sample, and relative to the magnetization generated throughout the sample in the second experiment. When zero or even number of 180° pulses are executed, the magnetization ends up along the positive longitudinal axis, whereas during a scan with odd number of 180° pulses, the magnetization ends up along the negative longitudinal axis. Thus, the 90° pulse after even or odd number of 180° pulses will excite the magnetization to positive or negative y axis, respectively. Further, adding and subtracting the individually stored scans with even and odd number of 180° pulses, respectively, will constructively accumulate signal from the desired locations, while destructively cancelling signal from all other locations. Table 2 shows how the amount of experiments with varying 180° pulse-gradient combinations affects on signal accumulation.

The number of component experiments required for n-dimensional selection is 2^n and thus volume selection requires eight acquisitions. This results in cancellation of signal outside a cuboidal volume defined by the intersection of the three selected slices.

Table 2: Experiments 1-8 of ISIS sequence with different gradient combinations (G_x,G_y,G_z) and corresponding signal accumulation. ON refers to the application of a selective pulse and OFF to the absence of selective pulse. V is a total volume without selection, S_n is a slice defined by field gradient along n-axis, L_{nm} is a bar (intersection of two slices in orthogonal planes) defined by gradients along n- and m- axis, and C_{nml} is a cube defined by gradients along n- m- and l-axis.

	$180°/G_x$	$180°/G_Z$	$180°/G_Z$	SIGNAL
exp 1	OFF	OFF	OFF	V
exp 2	ON	OFF	OFF	$V - 2S_X$
exp 3	OFF	ON	OFF	$V - 2S_Y$
exp 4	OFF	OFF	ON	$V - 2S_Z$
exp 5	ON	ON	OFF	$V - 2S_X - 2S_Y + 4L_{XY}$
exp 6	ON	OFF	ON	$V - 2S_X - 2S_Z + 4L_{XZ}$
exp 7	OFF	ON	ON	$V - 2S_Y - 2S_Z + 4L_{YZ}$
exp 8	ON	ON	ON	$V–2S_x–2S_y–2S_z+4L_{xy}+4L_{xz}+4L_{yz}+8C_{xyz}$

2.3 Magnetic resonance spectroscopy

In this section, the basic sources of fine structure of NMR spectrum is discussed. As an example the MRS spectrum of ATP is shown in Figure 5.

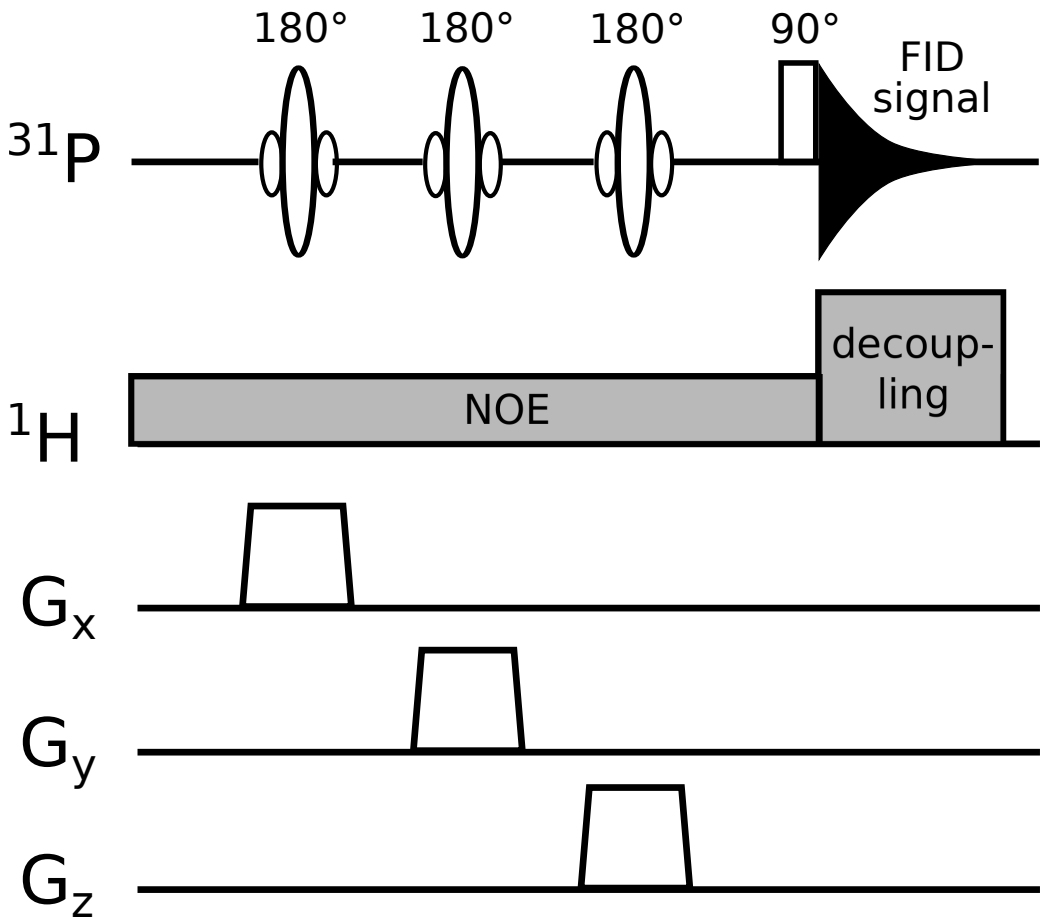

Figure 4: Structure of ^{31}P ISIS pulse sequence incorporated with nOe and proton decoupling.

2.3.1 Chemical shift

When a nucleus is placed in an external magnetic field, negatively charged electrons will rotate about B_0 in an opposite sense to the proton spin precession. Rotating electrons can be regarded as small currents, giving rise to a magnetic moment μ_e at the nucleus. μ_e opposes the external magnetic field and the effective field at the nucleus is reduced, thereby leading to a different Larmor frequency:

$$\nu = \frac{\gamma}{2\pi} B_0 (1 - \sigma), \tag{28}$$

where σ is the shielding constant, a dimensionless number, caused by the electrons surrounding a nucleus.

Usually chemical shifts δ are expressed in terms of parts per million (ppm) instead of Hertz; this expression is independent of the external field strength. Chemical shifts in ppm are defined as:

$$\delta = \frac{\nu - \nu_{ref}}{\nu_{ref}} \times 10^6, \tag{29}$$

where ν and ν_{ref} are the frequencies (in Hertz) of the compound under investigation, and of a reference compound, respectively.

By convention, the PCr resonance, albeit not present in the human liver, is used as an internal chemical shift reference and is assigned a chemical shift of 0.00 ppm. By a convention in NMR, the chemical shift δ scale always increases from right to left in plotted spectra.

Without this phenomenon nuclei of the same element in different molecule would resonate at the same frequency and the NMR spectroscopy would be of minor importance in chemistry, medicine or any other field.

2.3.2 J-coupling

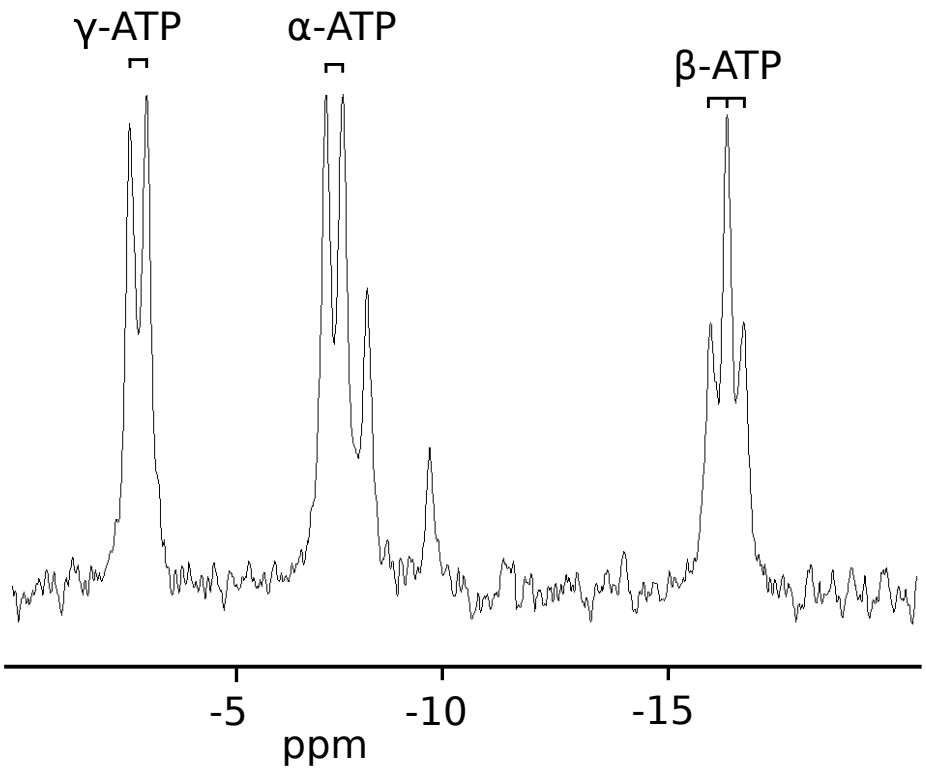

Figure 5: ATP resonances in simulated ^{31}P MR spectra. γ- and α- phosphates are coupled to β-phosphate only and appear as douplets. β-phosphate in the middle of the molecule is coupled to both neighbouring γ- and α- phosphates and therefore its resonance appears as a tripled.

A common feature of NMR spectra is the splitting of resonance into several smaller lines. This phenomenon is referred to as scalar coupling, J-coupling, spin-spin coupling, or the indirect dipole-dipole coupling. J-coupling originates from the magnetic moments, which can influence each other through indirectly through chemical bonds. As a contrary to dipolar coupling, interactions through chemical bonds will not average out, but give a rise to the J-coupling. The J-coupling con-

stant rapidly decreases with increasing number of chemical bonds. J-coupling can be typically ignored for four or more bonds. Unlike chemical shift, J-coupling is independent of the applied external magnetic field B_0 and therefore always specified in Hertz.

In ^{31}P NMR, homonuclear ^{31}P-O-^{31}P interactions stretch over two bonds, while heteronuclear ^{1}H-^{31}P interactions stretch over one bond only. When the frequency difference $|\nu_A - \nu_B|$ between two J-coupled spins A and B is much larger than the coupling constant J_{AB} between them, the splitting pattern can be predicted from the Pascal's triangle, which is shown in Table 3. This condition, $|\nu_A - \nu_B| \gg J_{AB}$, is certainly valid for heteronuclear J-coupling. However, for many homonuclear interactions the frequency difference $|\nu_A - \nu_B|$ is the same order of magnitude as the J-coupling constants J_{PH}, giving rise to a so-called strongly coupled spin systems. Magnetically equivalent nuclei do not produce observable splitting. Figure 5 shows an example of J-coupling of ATP.

Table 3: Pascal's triangle, used for splitting patterns between J-coupled spins.

No. of neighbors	relative intensities	pattern
0	1	singlet
1	1 1	doublet
2	1 2 1	triplet
3	1 3 3 1	quartet
4	1 4 6 4 1	pentet
5	1 5 10 10 5 1	sextet

At B_0 of 3.0 Tesla, the frequency differences of ATP resonances $|\nu_\gamma - \nu_\beta|$ and $|\nu_\beta - \nu_\alpha|$ are approximately $28J_{\gamma\beta}$ and $45J_{\beta\alpha}$, respectively. Therefore ATP-resonances can be considered as a weakly coupled spin system. The three-bond heteronuclear J-couplings for the PME and PDE resonances are in the 6–7 Hz range and lead to undesirable line-broadening. Line-broadening induced by heteronuclear J-coupling can be eliminated by heteronuclear decoupling, which will be discussed later in more detail.

Typical magnitudes of scalar coupling constants are: ^{1}H-^{31}P, 10−20 Hz; and ^{31}P-O-^{31}P, 15−20 Hz [57]. J-coupling phenomenon can be efficiently utilized in *in vitro* NMR spectroscopy experiments giving us information about molecular structures.

2.3.3 Proton-decoupling

The J-splittings distribute the signal intensity over many smaller peaks. These multiplet structures decrease the spectral resolution as the spectrum is crowded and more difficult to interpret. Moreover J-coupling decreases signal-to-noise ratio and therefore makes it undesirable phenomenon in *in vivo* NMR spectroscopy. For example, in hepatic ^{31}P MRS, separation of heteronuclearly coupled (^{31}P-^{1}H) PME and

PDE resonances into their subcomponents is impossible at clinical field strengths of 1.5-3.0 Tesla. However, occasionally well known multiplet structures can be used for resonance recognition [58]. In hepatic ^{31}P spectra $\alpha-$ and $\gamma-$ATP resonances have a doublet structures, while the phosphorus nuclei at the center of the triphosphate, $\beta-$ATP, has a triplet structure. These couplings of ATP resonances are homonuclear of nature , since nuclei are coupled to neighboring phosphorus.

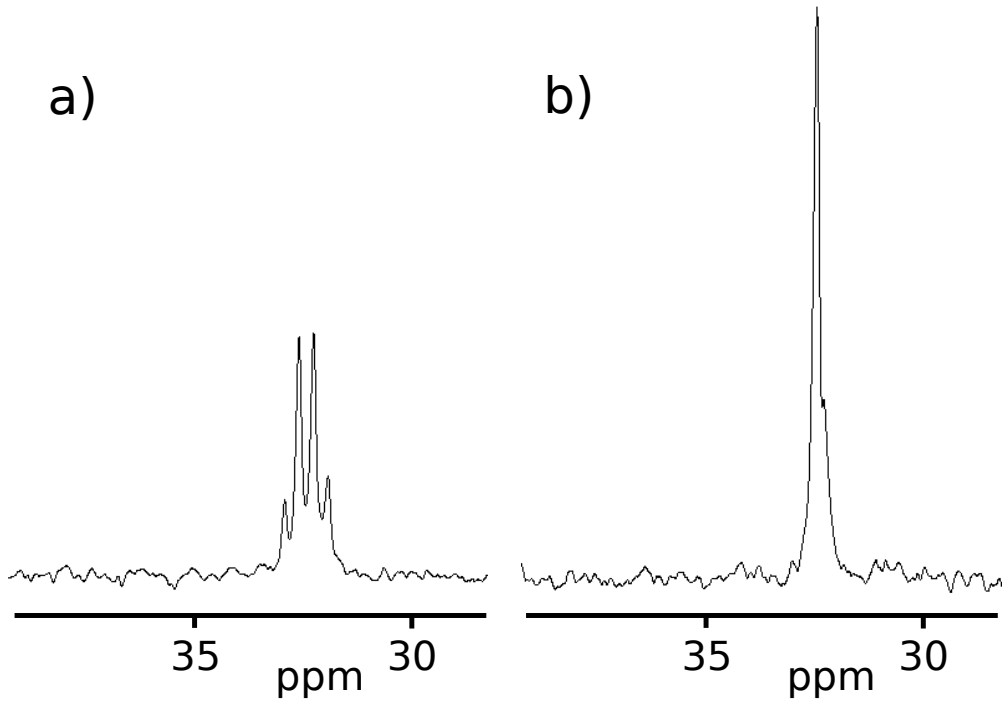

Figure 6: An example of ^{31}P MR spectra a) without and b) with proton-decoupling. Spectra are measured on a 10 cm diameter phantom sphere containing 313 mM methylphosphonic acid [$P(OH)_2O(CH_3)$]. Phosphorus nucleus is coupled to three methyl protons with J_{PH} of 17.24 Hz and the signal is splitted to quartet. By applying a proton-decoupling scheme to the measurement sequence, multiplet structure disappears and SNR is greatly improved.

The heteronuclear coupling effects discussed above can be removed by applying a proton decoupling scheme to the measurement pulse sequence. In this proton decoupling scheme, protons are irradiated during the ^{31}P acquisition. Figure 6 demonstrates the effect of decoupling scheme on spectral appearence.

Nuclear Overhauser enhancement and heteronuclear decoupling schemes can be incorporated into ISIS sequence as shown in Figure 4.

For phosphomonoesters, phosphodiesters, and ATP, the predominant phosphorous-proton J-coupling is to -O-CH2 methylene protons, which resonate at 4.3 ppm to 3.8 ppm.

2.3.4 Nuclear Overhauser effect

The nuclear Overhauser effect (nOe) requires the presence of two non-indentical spins and is closely related to magnetic dipolar interactions. For heteronuclear experiments, nuclear Overhauser effect generates useful enhancement in signal intensity of the low-sensitivity nucleus upon the saturation of the protons. Enhancement is brought about by ^{1}H irradiation before the start of each experiment.

$$\epsilon_{NOE} = 1 + \frac{\gamma_{^1H}}{\gamma_{^{31}P}} \frac{W_2 - W_0}{W_0 + 2W_{^{31}P} + W_2} = 1 + \eta, \tag{30}$$

where W_2 and W_0 are transition probabilities for double and zero quantum transitions, respectively. $W_{^{31}P}$ is transition propability for phosphorus spin.

Theoretical maximum of ϵ_{NOE} is achieved with very rapid molecular motion in extreme narrowing limit ($\omega^2\tau_c^2 \ll 1$):

$$\epsilon_{NOE} = 1 + \frac{\gamma_{^1H}}{2\gamma_{^{31}P}} = 1 + \eta, \tag{31}$$

where η is usually called nuclear Overhauser enhancement.

In theory, the maximal nOe for ^{31}P-^{1}H is 2.235, but the maximum η occurs in the extreme narrowing limit if the only relaxation mechanism is dipolar coupling. In practice, dipolar interactions account only for a part of all relaxation mechanism and thus typical nOe values with *in vivo* applications are 1.4-1.8 for ^{31}P-^{1}H [48].

The NOE factors for the metabolites are not all the same. It has been shown that T1 values correlate with NOE enhancement (η). Metabolites, sensitive to relaxation mechanisms other than dipolar interactions, have shorter T1 and smaller η. Estimated NOE enhancement, by Li *et al.* [59], for liver metabolites at 1.5 Tesla are shown in Table 4. However, enhancement is expected to be smaller at 3.0 Tesla, where weighting of CSA as a relaxation mechanism increases.

2.4 Processing of the NMR signal

NMR signals can be prosessed and quantified either in a time or a frequency domain. Typically, signals are preprocessed prior to quantification in order to correct the signal phase or baseline, reduce noise, improve the spectral resolution and suppress unwanted resonances. These analysis steps are discussed in the following sections.

2.4.1 Zero filling

The spectral resolution Δv of a NMR spectrum is SW/N, where SW is spectral width, N the number of sampled points and also inversely proportional to the sampling time T_{acq}:

$$\Delta v = \frac{1}{T_{acq}} = \frac{1}{N\delta t}, \tag{32}$$

where δt is the time interval between two successive sampling points. Thus, spectral resolution can be improved by increasing the acquisition time or decreasing

Table 4: Estimated contributions of nOe (η) for each metabolite in hepatic ^{31}P NMR spectra at 1.5 Tesla by Li *et al.* [59]

Compound	NOE
Phosphoethanolamine (PE)	0.30
Phosphocholine (PC)	0.47
Inorganic phosphates (Pi)	0.17
Glycerophosphoethanolamine (GPE)	0.59
Glycerophosphocholine (GPC)	0.73
Phosphoenylpuryvate (PEP)/phosphatidylcholine (PtdC)	0.34
Adenosine triphosphate (α-ATP)	0.36
Adenosine triphosphate (γ-ATP)	0.21
Adenosine triphosphate (β-ATP)	0.21
Nicotinamide adenine dinucleotide phosphate (NADPH)	0.55

the spectral width. However, in order to avoid aliasing, Nyqvist-Shannon sampling theorem set limits to minimum spectral width, and, on the other hand, increase of acquisition time will lead to an increase of relative noise contribution. Similar effects can be achieved through signal processing. An operation of adding a string of time points with zero amplitude to the FID, prior to Fourier transformation is known as zero filling. This operation simulates extending of the acquisition time. Zero filling does not increase the information content of the data, but it can greatly improve the spectral appearance as shown in Figure 7.

As an opposite to zero filling, few first points of the FID can be be removed before Fourier transform. This can be used to suppress wide spectral resonances with very short T2.

2.4.2 Time domain filtering

Spectral apodizing can be used for line broadening or noise reduction. In order to optimize SNR, optimal line broadening to use is the line width at half maximum (LWHM). Increasing the width of the window function, will reduce spectral resolution. Typical window functions used in *in vivo* MR spectroscopy include Hamming, Hann, Gaussian and exponential functions. Exponential weighting is done by multiplying FID with a following function:

$$f(t) = e^{-t/T_w}, \tag{33}$$

where T_w (> 0) is a time constant, which determines the steepness of the decay. Filter function $f(t)$ will enhance the data points at the beginning of the FID.

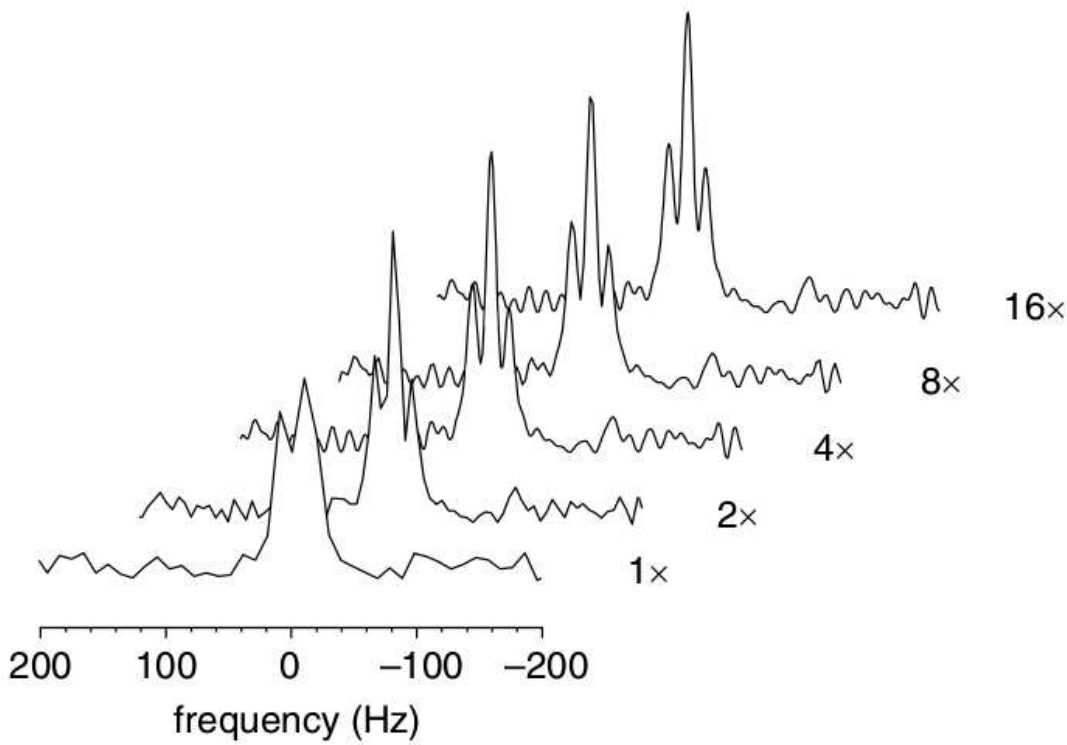

Figure 7: Effect of zero filling on spectral resolution. With spectral resolution of 9.77 Hz, triplet structure of β-ATP is not well resolved. Zero filling the original spectra prior to Fourier transform by factors 2, 4, 8 and 16 leads to spectral resolutions of 4.89, 2.44, 1.22 and 0.61 Hz, respectively. Triplet structure is already resolved after zero filling by factor of 2, but no further improvement in spectral resolution is observed by increasing the factor above 4. Figure taken from [57].

whereas, the end parts of the FID, where noise is dominating, will be damped and the SNR of the spectrum is enhanced. T_w of 200 ms corresponds 5 Hz.

Theoretically predicted Lorentzian lineshape has longer 'tails' than Gaussian lineshape. If an accurate determination of overlapping resonance lines is required, it might be advantageous to convert Lorentzian NMR lineshape to more narrow Gaussian lineshape:

$$f(t) = e^{t/T_L} e^{-t^2/T_G^2}, \tag{34}$$

where T_L and T_G are time constants for Lorentzian and Gaussian filtering, respectively. Lack of negative sign in the exponent of the first term will decrease the Lorentzian part of the FID, while the second term increases (assuming that $T_G > 0$) the Gaussian character of the FID.

Figure 8 shows clear improvement in noise reduction in hepatic *in vivo* ^{31}P MR spectrum, where LWHMs for GPC and GPE are $\tilde{9}$-10 Hz due to apodization with different Lorentzian filters.

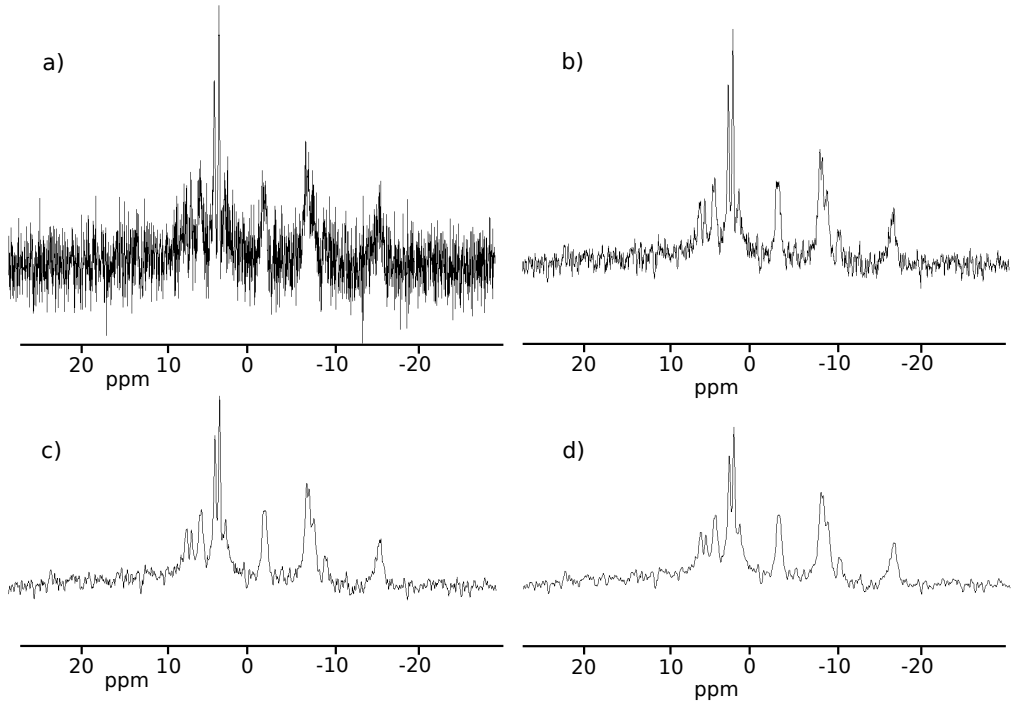

Figure 8: *In vivo* ^{31}P MR spectrum of the human liver a) without spectral apodization and with spectral apodization with Lorenzian filters of b) 10 Hz, c) 20 Hz and d) 30 Hz.

2.4.3 Fourier transform

Fourier transform does not enhance the information content, but makes the information in the signal more visible for the human eye. Both time domain signal s(t) and the spectrum S(ω) are complex functions. While time-domain signal is a superposition of oscillating components, the spectrum is a superposition of Lorentzian spectral components. The imaginary part of the complex Lorentzian function is called the dispersion Lorentzian:

$$S(\omega) = \frac{\omega - \omega_0}{\lambda^2 + (\omega - \omega_0)^2}, \tag{35}$$

where ω_0 is the angular Larmor frequency, ω the frequency coordinate and λ is a peakwidth parameter. The real part of the complex Lorentzian is called the absorption Lorentzian:

$$S(\omega) = \frac{\lambda}{\lambda^2 + (\omega - \omega_0)^2}. \tag{36}$$

Since absorption Lorentzians have better resolution than dispersion Lorentzians, only the real part of spectrum is usually displayed (Figure 9). The parameter λ is

called the coherence decay rate constant equal to the inverse of transverse relaxation rate constant T_2

$$\lambda = \frac{1}{T_2} \tag{37}$$

From the Equations 37 and 36 above can be seen that resonances with fast and slow signal decay will lead to a broad and narrow spectral peaks, respectively. In practice Fourier transforms are calculated using an efficient numerical algorithm called the fast Fourier transform (FFT) [60]. An important limitations of FFT is that a number of Fourier-transformed points must be an integer power of 2.

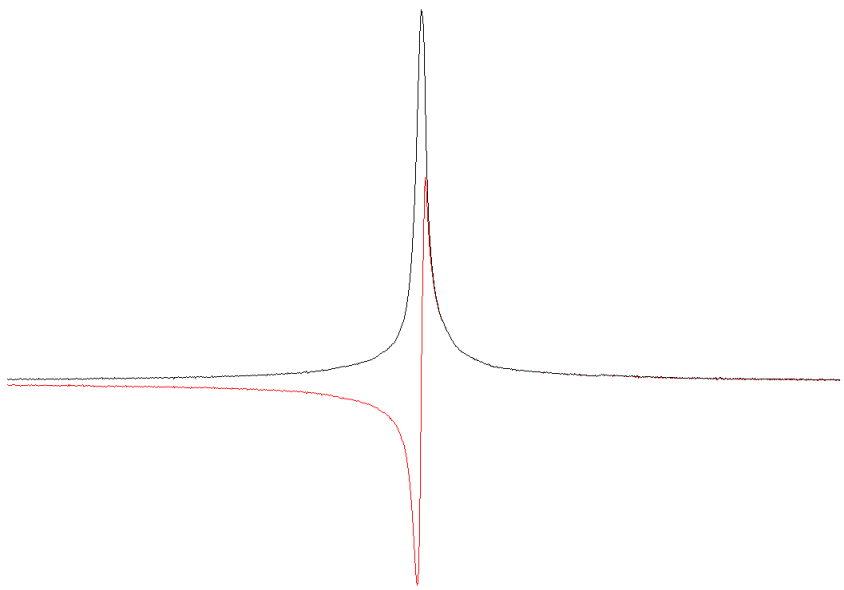

Figure 9: Absorption Lorentzian (black line) and dispersion Lorentzian (red line)

2.4.4 Phase Correction

Macroscopic motion can lead to zero order phase changes. Phase changes do not necessary lead to signal loss *per se*, but it can be problem at case of extensive signal averaging of spectra with different phases. Phase correction prior to signal averaging is therefore highly recommended.

usually phase correction is performed according to:

$$\varphi(\omega) = \varphi_0 + \varphi_1\omega, \tag{38}$$

where subscripts 0 and 1 indicate zero (constant) and first order phases, respectively. φ_0 is constant phase correction for all resonances in the spectra and φ_1 is a linear, frequency dependent phase correction. Figure 10 shows an example of the effect of phase correction on spectrum appearance.

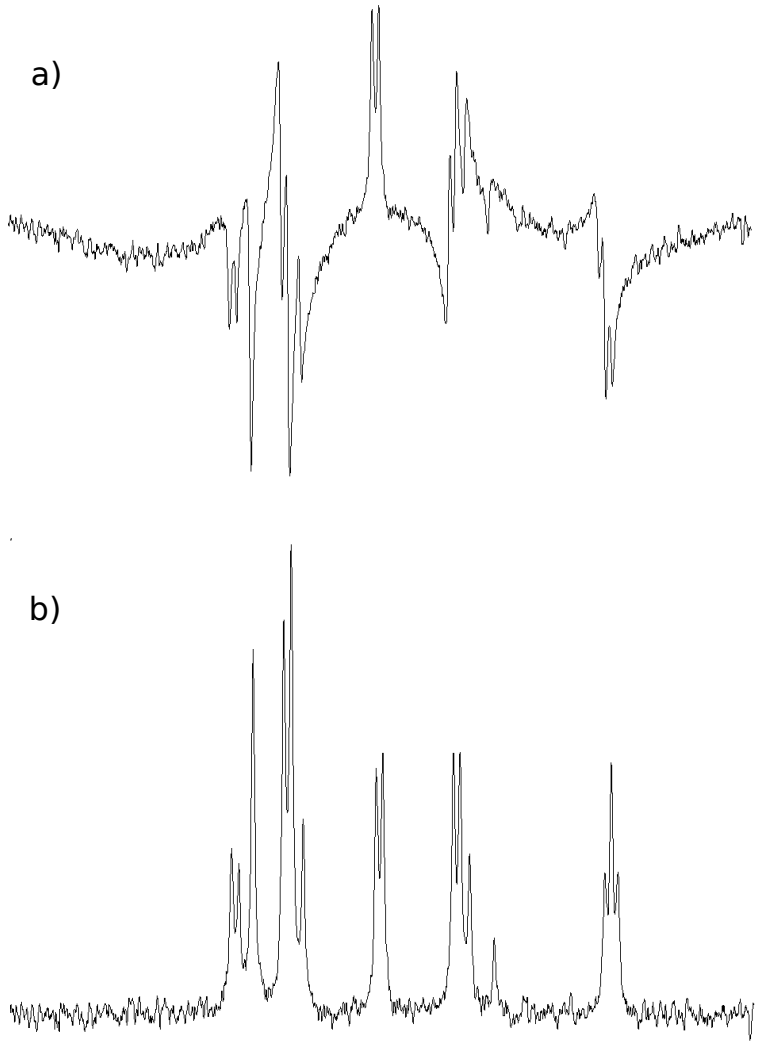

Figure 10: The effect of signal phase on spectral appearence: a) dephased simulated ^{31}P MR spectrum and b) same spectrum corrected for first and second order phases.

If the first points of a time domain signal were truncated, this has an influence on the first order phase or begin time of the signal that has to be corrected.

2.4.5 Quantification

Instead of reporting signal intensities in voltage or arbitrary units, *in vivo* NMR spectra can be used to derive absolute concentrations, expressed in mmol/L or μmol/g of tissue. This originates from the fact that net magnetization M_0 is directly proportional to the number of spins, which is proportional to the molar concentration. However, in MRS experiment, M_0 is not detected directly but rather an induced current proportional to the transverse magnetization. The induced signal S_M from a metabolite M detected in a receive coil is depended of several factors as

follows:

$$S_M = NS \times RG \times \omega_0 \times [M] \times V \times f_{sequence} \times f_{coil}, \tag{39}$$

where NS represents number of scans, RG receiver gain, ω_0 Larmor frequency and V volume. Sequence factor ($f_{sequence}$) depends on the TE, TR, spatial localization method, as well as T_1 and T_2 of the measured metabolite M. Coil factor f_{coil} depends on the qualities of the RF coil *e.g.* quality factor Q, filling rate and geometry of the coil.

Several methods exist for quantification of metabolite in NMR spectroscopy. These can roughly be divided in time or frequency domain methods. In this thesis, a model based approach called AMARES was used. Other methods such as peak area integration in frequency domain are only briefly described.

Integration of the peak area is the most straightforward method to calculate peak intensities in the frequency domain, but it is not suitable for overlapping peaks. In addition, it cannot take tails into account and thus intensities are systematically underestimated. Figure 11 demonstrates the determination of γ-ATP intensity by integration.

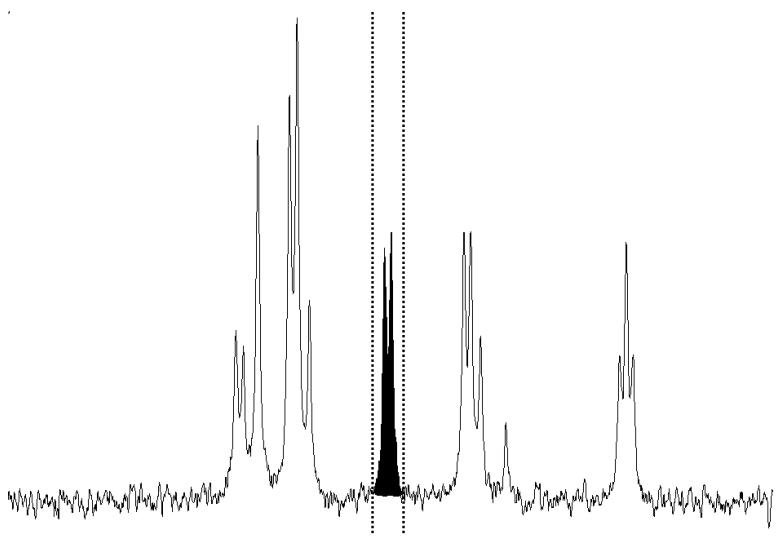

Figure 11: The intensity of γ-ATP determined by integration between vertical dashed lines in phase corrected spectrum.

Prior knowledge of relations between model parameters decreases the Cramer-Rao bounds (CRB) and consequently increases the precision. Partially overlapping resonances cannot be separated by integration.

2.4.6 Error estimation

Error estimation is an important part of metabolite quantification. If noiseless data can be exactly modelled, measured data x_i can be expressed as

$$x_i = \hat{x}_i + b_i, \tag{40}$$

where $\hat{x}_i$ is model function and b_i Gaussian distributed noise [61]. Evaluation of the CRLBs requires inversion of the Fisher information matrix F, which can be expressed as

$$F = \frac{1}{\sigma^2}\Re(P^T D^H DP), \tag{41}$$

where σ is the standard deviation of real and imaginary parts of the noise, $\Re$ refers to real part. T and H are transposition and Hermitian conjugation, respectively. The matrix D contains the partial derivatives of the model function $\hat{x}_i$ with respect to the parameters p_j in the vector p:

$$D_{ij} = \frac{\partial x_i}{\partial p_j} \tag{42}$$

The prior knowledge matrix P can be expressed as:

$$P_{mn} = \frac{\partial p_j}{\partial p_k^{'}}, \tag{43}$$

where p_k corresponds to the unconstrained parameters p_j to be estimated. Incorporation of prior knowledge reduces the number of free parameters and consequently the size of information matrix F.

The CRBs on the standard deviations of the estimated parameters are given by the fundamental Cramér-Rao inequality, which is obtained from inverting the Fisher matrix as follows:

$$\sigma_{p_i} \geq CRLB_{p_i} = \sqrt{F_{ii}^{-1}} \tag{44}$$

Precision of the quantification cannot supersede the CRLBs, but small CRLB is not a guarantee for an accurate metabolite concentration.

2.5 The liver and ^{31}P metabolites

In this section, anatomy and physiology of liver is first described. Further, metabolites visible in hepatic *in vivo* ^{31}P MR spectroscopy are presented.

2.5.1 Liver anatomy

Liver consists of four anatomically distinct lobes shown in Figure 12: the right, left, quadrate and caudate lobes in an ascending size order.

In a histological scale, liver consists of functional units called liver lobules. These lobules are formed by paranchymal and nonparenchymal cells. Parenchymal cells called hepatocytes occupy approximately 80 % of the total liver volume. They perform most of the numerous liver functions. Nonparenchymal cells, locating in the sinusoidal compartment of the tissue, consist of three different types of cell types:

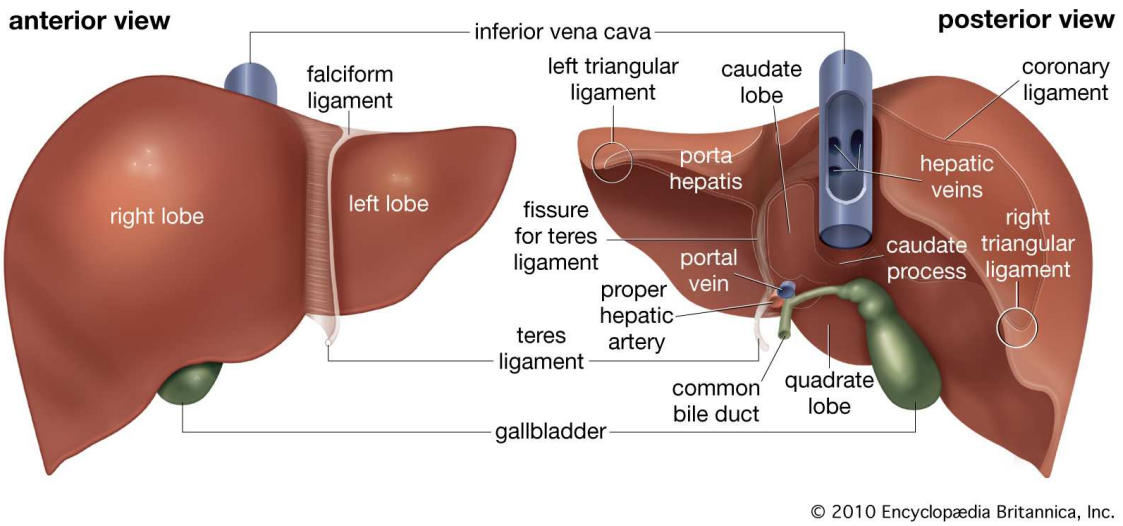

Figure 12: Anatomy of the liver. Picture taken from [62].

Kuppfer cells, sinusoidel endothelial cells and hepatic stemmate cells. Nonparenchymal cells represent 40 % of the total number of cells in the liver, but contribute only 6.5 % of the total liver volume [63].

A whole network of various sized ducts branch through the liver. This structure is known as a biliary tree and it has an important role in transporting the bile. Bile, needed for digestion of food, contains water, electrolytes and organic molecules including bile acids, cholesterol, phospholipids and bilirubin. Bile is produced in hepatocytes and it drains into microscopic canals known as bile canaliculi. These bile canaliculi join together into larger bile ducts known as canals of Hering, from which the path goes as follows in ascending order of the duct size: interlobular bile ducts, intrahepatic bile ducts, and left and right hepatic ducts, which merge to form the common hepatic duct that exits the liver and joins cystic duct. The structure of the biliary tree, excluding smaller structures, is shown in Figure 13.

Compared to other organs, liver has a unique, dualistic, blood supply system. Oxygeneted blood is provided by hepatic arteries, just like for any other organ, but it represents only one third of the total blood supply of the liver. Two thirds of the blood is provided by the hepatic portal vein, which carried nutrient-rich venous blood drained from spleen, stomach, pancreas, gallbladder and intestine. The liver receives 25 % of the cardiac output even though it constitutes only approximately 2.5 % of the body weight, and the hepatic parenchymal cells are the most richly perfused of any of the organs [65].

Right liver lobe is the most obvious target for volume of interest in single voxel spectroscopy. It is 5 to 6 times larger and less sensitive to cardiac motion as compared to the left lobe. Liver steatosis has been reported to be greater in the right than in the left lobe, but generally the lobar variability of the steatosis is low [66]. Therefore, the right lobe is a primary target for monitoring liver metabolism.

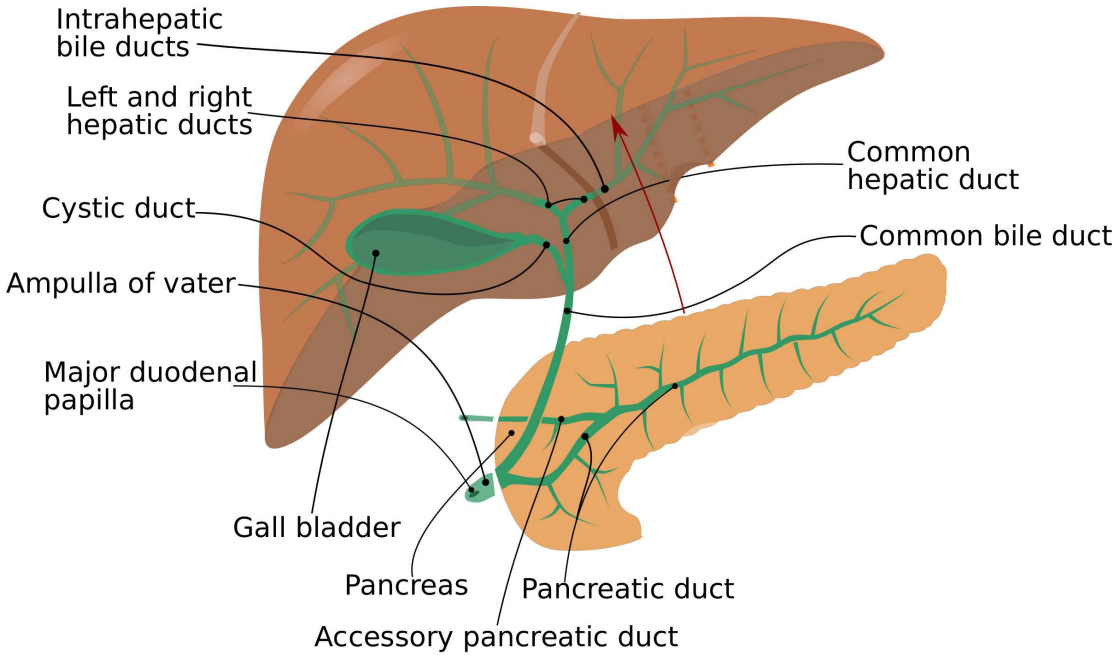

Figure 13: Biliary tract. Figure modified from [64]

2.5.2 Liver physiology

Liver has numerous important functions in human physiology such as ingestion, metabolism, detoxification, storage, production and immunity.

Moreover, liver has a critical role in metabolism of different energy sources. In maintenance of normal blood glucose levels, excess postprandial glucose entering the blood is taken up by the liver and sequestered and stored as a glycogen in a process called glycogenesis. When glucose levels in blood begin to decline glycogen is depolymerised into glucose and exported back to blood. When glycogen reserves become exhausted glucose can be synthesized in the liver from e.g. amino acids in a process called gluconeogenesis.

In fat metabolism, liver is active in oxidizing triglycerides to produce energy. Liver synthesises fatty acids from excess carbohydrates in a process known as *de novo* lipogenesis. Also, large quantities of cholesterol and phospholipids are synthesised in the liver.

Liver takes part in protein metabolism by synthesising i) most of the plasma proteins, ii) non-essential amino acids and iii) clotting factors necessary for blood coagulation. Liver also removes toxic ammonium from circulation by synthesising urea.

In digestion of fat, liver produces bile, which helps emulsification of fats for absorption of fatty acids.

Table 5: Chemical shifts and coupling constants of relevant ^{31}P containing metabolites in the human liver [67, 68]

Compound	Shape	Chemical shift (ppm)	J-coupling (Hz)
Phosphoethanolamine (PE)	singlet		-
Phosphocholine (PC)	singlet	5.88	-
Inorganic phosphates (Pi)	singlet	5.02	-
Glycerophosphoethanolamine (GPE)	singlet	3.20	-
Glycerophosphocholine (GPC)	singlet	2.76	-
Phosphoenylpuryvate (PEP)	singlet	2.06	-
Adenosine triphosphate (α-ATP)	doublet	–7.52	15.5-19.5
Adenosine triphosphate (γ-ATP)	doublet	–2.48	15.5-19.5
Adenosine triphosphate (β-ATP)	triplet	–16.26	15.5-19.5
Nicotinamide adenine dinucleotide phosphate (NADPH)	singlet	-8.30	-

In addition, liver clears blood of drugs and other (harmful) substances like alcohol and helps immune system by producing immune factors and removing bacteria from the bloodstream.

Dispersion of the phosphates found *in vivo* is relatively large - approximately 30 ppm - which makes spectral resolution sufficient to distinquish most of the key metabolites at clinical field strenghts ($\leq$ 3.0 T). In a standard clinical environment with standard sequencies, ^{31}P MRS detects relatively few spectral signals. These resonance singnals are phosphomonoesters (PME), inorganic phophate (Pi), phosphodiesters (PDE), nucleoside triphosphate (γ-NTP), α-NTP, β-NTP. All of these signal names by themselves do not necessarily carry descriptive value in biochemistry, physiology, or pathophysiology. Rather, they represent a heterogenous mix of compounds that share a common chemical feature (i.e. phosphomono- or phosphodiester bond)[69].

2.5.3 Phosphomonoesters

According to *in vitro* NMR studies at high field strenghts (11.7 Tesla), phosphomonoester region of the hepatic *in vivo* MR spectrum contains over 10 overlapping resonances including signals from adenosine monophosphate (AMP) [71], Phosphoethanolamine (PE), Phophocholine (PC), coenzyme A, 2,3-diphosphoglycerate (2,3-DPG), and intermediates of carbohydrate metabolism such as glucose 6-phosphate, glycerol 1-phosphate, 3-phosphoglycerate, and ribose 5-phosphate (Figure 14b). Figure 15 shows a PME region of the high-resolution *in vitro* spectra of human liver

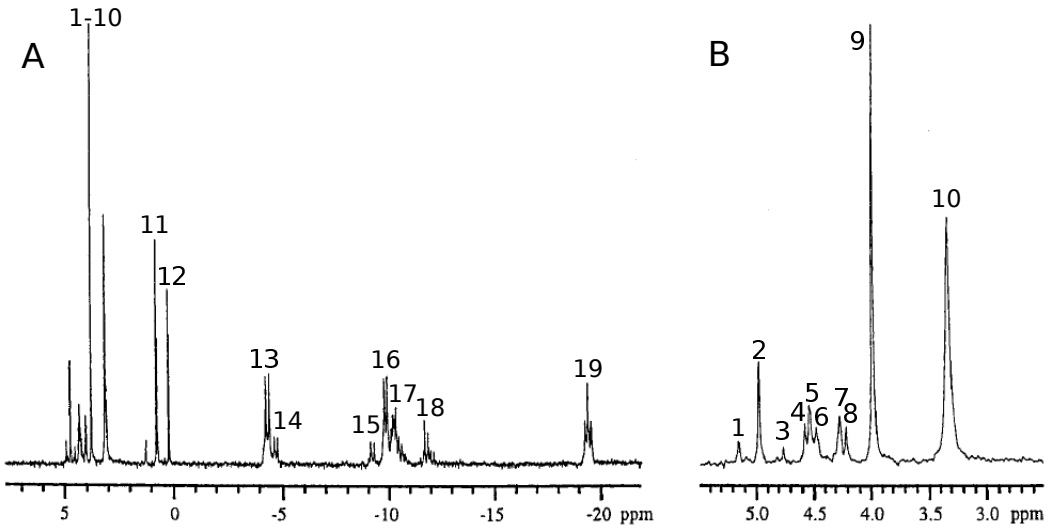

Figure 14: *In Vitro* ^{31}P NMR spectrum at 121.4 MHz of perchloric acid liver extract of A) healthy rat and B) expanded view between 5.5 and 2.5 ppm. Metabolites: 1, glucose-6-phosphate; 2, *sn*-glycerol 3-phosphate; 3, coenzyme A; 4, fructose 6-phosphate; 5, Phosphoethanolamine; 6, adenosine monophosphate; 7, NADPH; 8, 2,3-diphosphoglycerate; 9, phosphocholine; 10, inorganic phosphate; 11, glycerophosphoethanolamine; 12, glycerophosphocholine; 13, γ-NTP, 14, β-ADP; 15, α-ADP; 16, α-ATP; 17, NADPH; 18, UDP-glucose; 19, β-NTP. Edited from the paper by Harvey *et al.* [70]

extracts. Excluding PE and PC, most of these metabolites are unstable with ischaemia and their concentrations can change by ischemic periods up to one hour. These ischaemia sensitive metabolites cannot be studied *in vitro*. PME metabolites, in particular PC and PE, are believed to represent phospholipid cell membrane precursors [69]. PE and PC represent 7 and 24 % of the total lipid composition of liver plasma membrane, respectively [72]

2.5.4 Phosphodiesters

Phosphodiesters (PDE) refer metabolites with phosphodiester bond. In the human liver PDE region contains two major resonances: glycerophosphocholine (GPC) at 3.20 ppm and glycerophosphoethanolamine (GPE) at 2.76 ppm. Both of these are thought to represent cell membrane degradation products [69].

2.5.5 Inorganic phosphates

Inorganic phosphate (Pi), shown in Figure 16, is a small and symmetric molecule. It resonates as a singlet between phosphomonoesters and phosphodiesters at 5.02 ppm. Inorganic phosphates are released by the hydrolysis of ATP and ADP or other nucleoside diphosphates and triphosphates.

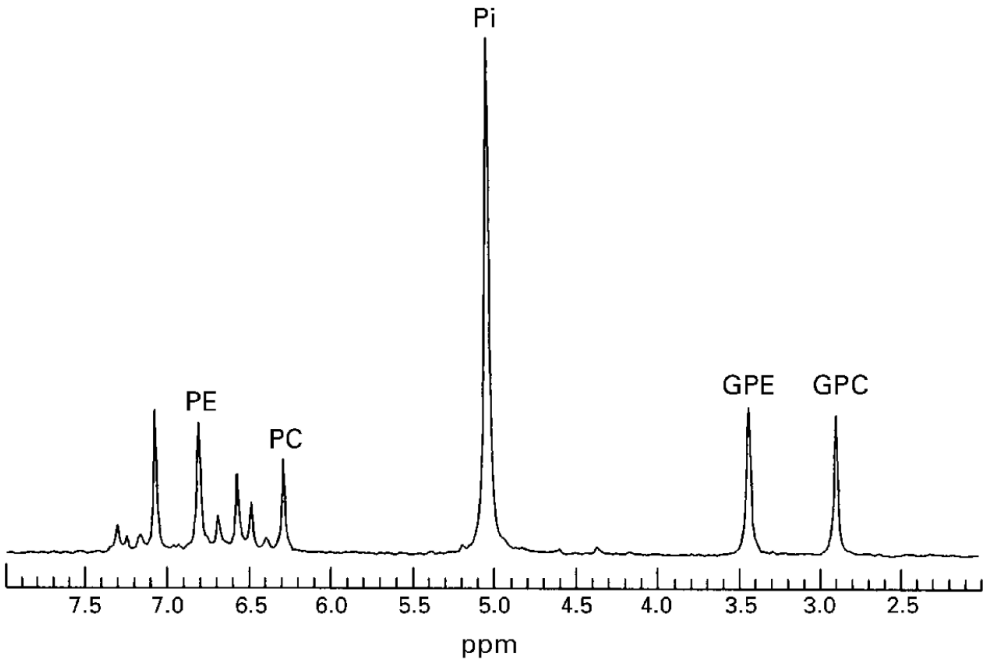

Figure 15: *In Vitro* ^{31}P NMR spectrum of the sample from human liver measured at 11.7 Tesla. Downfield side (ppm ≤ 2.00) of the spectrum has been excluded from the original figure [73].

In *in vivo* MRS, the quantification of Pi, is hampered by partly overlapping resonances of PME and PDE, and wide underlying resonance from motion restricted phospholipids and vesicle bilayers [74, 75, 76].

The chemical shift of Pi is sensitive to pH and therefore the chemical shift of Pi can be used to calculated pH by utilizing Henderson−Hasselbach equation :

$$pH = 6.75 + log\left(\frac{\delta - 0.75}{3.35 - \delta}\right), \tag{45}$$

where δ is the chemical shift in ppm for the Pi resonance [67].

2.5.6 Phosphoenolpuryvate and phosphatidylcholine

A small resonance usually seen in *in vivo* liver NMR spectra on upfield side of PDE at 2.06 ppm, has been conventionally assigned to phosphoenolpuryvate (PEP) [77, 78]. PEP is an important chemical compound, which is involved in glycolysis and gluconeogenesis. The conversion of PEP to ADP by puryvate-kinase generates one molecule of puryvate and one molecule of ATP. Reversed phophorylation of puryvate to PEP by phosphoenolpyruvate-carboxykinase is considered to be a rate-limiting step in gluconeogenesis [79]. However, it has been suggested that intrahepatic 31P MRS signal at 2.06 ppm may represent both intrahepatic phosphatidylcholine (PtdC) and phosphoenolpuryvate [80]. PtdC is a typical phosphodiester

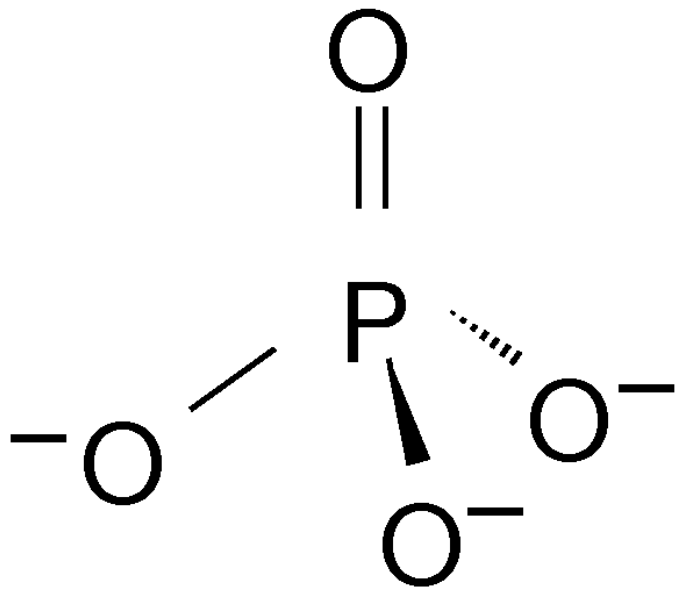

Figure 16: Tetrahedrally symmetric Pi molecule

and part of bile lecithin. PtdC synthesis is essential for secretion of very low density lipoproteins (VLDL) from the liver. Chemical shift of PEP has a strong dependence on the pH, while the chemical shift of PtdC is pH-independent. According to titration curve of PEP shown in paper by Chmelík *et al.* [81] , PEP would resonate at 2.06 ppm in an environment with pH of approximately 7.5.

2.5.7 Nucleoside triphosphates

Nucleoside triphosphate (NTP) include α, β and γ signals as shown in Figure 18. Resonance of α-NTP appears as a doublet at -7.52 ppm, β-NTP as a tripletat -

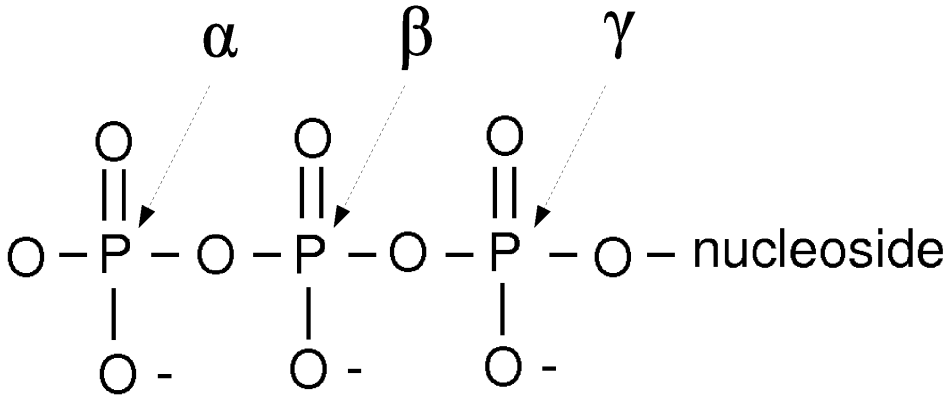

Figure 17: A structural formula of the nucleoside triphospate (NTP) molecule.

16.26 ppm and γ-NTP as a doublet at -2.48 ppm. Homonuclear coupling constants for NTP resonances are shown in Table 5.These nucleoside signals are commonly referred as ATP signals, although cytosine (CTP), guanosine (GTP), inosine (ITP) and uridine (UTP) triphosphates contribute to these signals more or less. *In vitro* studies suggest that ATP represents approximately 80 % of the total nucleoside triphosphate content in the rat liver [82]. On the other hand some ATP, less than 10 %, may not MRS visible due to binding to membranes or macromolecules, association to paramagnetic molecules or microviscosity [83].

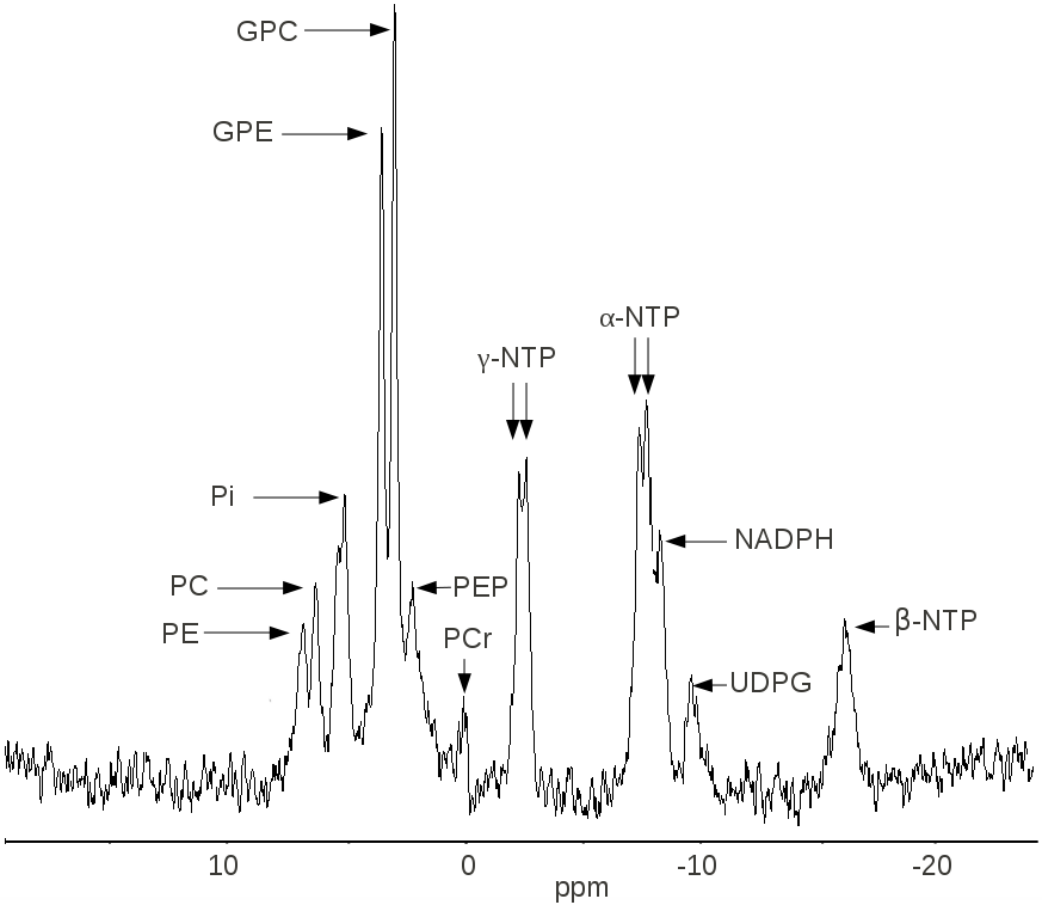

Figure 18: Hepatic ^{31}P MR spectrum averaged from six healthy valunteers. PE, phosphoethanolamine; PC, phosphocholine; Pi, inorganic phosphates; GPE, glyserophosphoethanolamine; GPC, glycerophosphocholine; PEP/PtdC, phosphoenolpuryvate/phosphatidylcholine; γ-NTP, γ-nucleosidetriphosphate; α-NTP, α-nucleosidetriphosphate; NADPH, nicotinamide adenine dinucleotide phosphate; UDPG, uridine diphosphate glucose; β-NTP, β-nucleosidetriphosphate.

2.5.8 Diphosphodiesters

In a high resolution ^{31}P NMR spectra of liver extracts from rats, there is a group of peaks centred at 10.4 ppm. This group of peaks is defined as a diphosphodiester-

region having contributions from all forms of nicotinamide adenine dinucleotides: NAD, NADH, NADP, NADPH. Another group of diphosphodiester resonances is centred at 12.0 ppm including uridine diphospho glucose (UDPG) [70].

2.5.9 Other metabolites and contamination from non-hepatic tissue

Vascular volume of the human liver is approximately 25 % [84], which makes contamination from blood practically impossible to avoid. Erythrocyte 2,3-diphosphoglycerate (2,3-DPG) resonates at 3,8 ppm and 2.8 ppm thus overlapping with Pi and PME. Occasionally, a small phosphocreatine resonating at 0.0 ppm can be seen in a hepatic ^{31}P MR spectra. Usually, this has been considered extra-hepatic contamination due to poor localization. However, it has been also suggested that small quantities of PCr is present in normal human liver [85]

Table 6: Parameters used for simulated ^{31}P MR spectra. A denotes amplitude; α Lorenzian damping factor; β, Gaussian damping factor; f, frequency (chemical shift). Zero order phase φ_0 and begin time t were both fixed to 0 for all peaks

Peak (nr)	A	α (Hz)	β (Hz)	f (Hz)
1	1.2	30	0–50	327
2	1.1	30	0–50	304
3	2.8	30	0–50	260
4	2.8	30	0–50	166
5	3.5	30	0–50	143
6	1.4	30	0–50	106
7	1.85	30	0–50	-118
8	1.85	30	0–50	-138
9	1.9	30	0–50	-355
10	1.9	30	0–50	-375
11	1.1	30	0–50	-429
12	0.5	30	0–50	-512
13	0.95	30	0–50	-820
14	1.9	30	0–50	-840
15	0.95	30	0–50	-860

3 Experiments

Experiments consist of simulations and actual human measurements. Simulated spectra were constructed to study the effect of spectral noise and line broadening on the reliability of signal quantification.

3.1 Simulations

^{31}P MR spectra were simulated using simulation tool implemented in jMRUI v3.0 software [86]. Relative concentrations for PE, PC, Pi, GPE, GPC, PEP, γ-ATP, α-ATP, NADPH and β-ATP were derived from the paper by Li et al. [59]. In addition, UDPG resonance was added. Chemical shifts (frequencies), coupling constants, and relative concentrations are shown in Table 5. Broad baseline resonance in phosphodiester region was not modelled. Example of simulated spectra are shown in Figure 19.

Each of 15 signal components, shown in Table 6, were created using following equation:

$$x(t) = Ae^{-\alpha-(\beta t)^2}e^{i(2\pi ft+\varphi_0)}, \tag{46}$$

where A represents signal amplitude (concentration), and α and β Lorentzian and Gaussian damping factors, respectively. Both, zero (φ_0) and first (begin time, t) order phases were set to 0.0 for each resonance. Transmitter frequency was set to 51.72 MHz, which corresponds the Larmor frequency of ^{31}P nucleus at 3.0 Tesla. Simulated spectra consisted of 4096 data points over the bandwidth of 3000 Hz. The variable α was set to 30 Hz and the value of β was varied in order to demonstrate the effect of inhomogeneous broadening.

In order to compare the performance of two fitting approach in the presence of random noise, 20 Monte Carlo simulations ($\alpha = 30$ and $\beta = 30$) with with 6 different noise levels (5, 10, 15, 20, 30 and 50%) were generated. These simulations were quantitated with Gaussian and Lorentzian lineshape fits. Average concentrations and coefficients of variations were determined.

Random noise with varying RMS amplitude was also added in order to test and demonstrate the effect of noise to reliability of the quantifications methods.

According to Equation 36, when simple monoexponential decay is expected resonance lineshapes are purely Lorentzian. However, this not the case in real life *in vivo* measurements. Residual eddy currents, magnetic field inhomogeneity and multi-exponential relaxation make line shapes more complex *in vivo*.

3.2 Measurements

All measurements were performed on a 3.0 Tesla (Achieva, Philips, Best, Neatherlands) clinical imager (Figure 20).

Phosphorus signals were measured using a ^{31}P transmit-receive loop coil with diameter of 14 cm (Figure 21). The system integrated body coil was used for proton decoupling and NOE irritation.

3.3 In vivo measurements

We measured 6 (one male) healthy subjects after an overnight fast. Three subjects were measured twice in separate occasion in order to determine inter-individual reproducibility.

A circular, non-flexible ^{31}P transmit-receive loop coil with a diameter of 14 cm (P-140) was placed laterally over the liver, parallel to the main magnetic field B_0. The coil placement was checked with the localizers and repositioned if necessary.

The ^{1}H body coil was used to collect T1-weighted ultrafast gradient-echo images with repetition time (TR), echo time (TE) and flip angle of 8 ms, 2.3 ms and 15°, respectively. Images were collected in three orthogonal directions with 10 mm slice thickness covering the whole liver in all directions. Image acquisition was performed in an end-exhalation by instructing the subjects to breath in, breath out and the hold their breath. Duration of each breath hold was approximately 20 seconds.

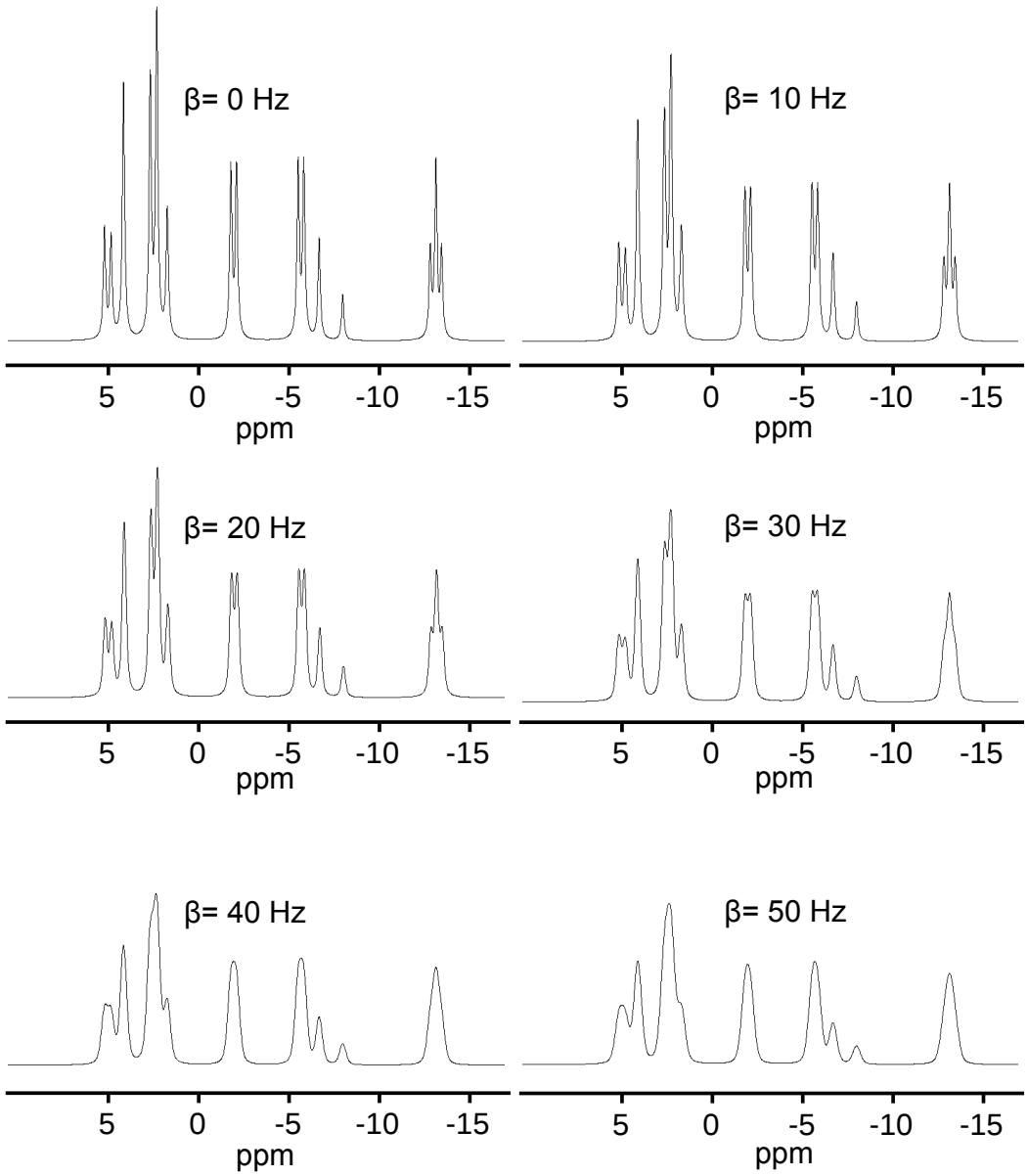

Figure 19: The panel of six simulated spectra demonstrates the effect of Gaussian broadening on spectral resolution and signal-to-noise ratio (peak hights). Resonances were simulated according to Equation 46. Lorentzian dumping factor (β) of a) 0 Hz, b) 10 Hz, c) 20 Hz, d) 30 Hz, e) 40 Hz, f) 50 Hz were used. More detailed simulation parameters are presented in Table 6.

3.4 ^{31}P MRS acquisition

A $6 \times 6 \times 6$ cm^3 voxel was placed in the center of the right liver lobe to avoid signal contamination from the surrounding tissues according to Figure 22.

A total of 2048 data points were acquired in 682 ms over a 3000 Hz receiver bandwidth resulting a spectral resolution of 1.46 Hz/point. The ISIS volume selection

Figure 20: Experiments were performed on a 3T clinical imager installed in Meilahti hospital.

method was used for 3D spatial localization with a TR of 6000 ms and 128 acquisitions. The more detailed structure of the ISIS sequence used in this experiment is shown in Table 2.

Spatial variation of B_1 associated with a transmit-receive surface coil was compensated by using frequency modulated adiabatic pulses. A hyperbolic-secant based adiabatic half-passage pulse (HS-EX) was used for the excitation, and the slice selection was carried out by using a hyperbolic-secant inversion pulse (HS). For the P-140 coil used in this experiment B_{1max} is set to 60 μT. To maximise the bandwidth, both pulses were time scaled such that their maximum B_1 matched the B_{1max} of the coil. Resulting pulse lengths T for the HS inversion and HS-EX detection pulses are 4.22 ms and 5.42 ms, respectively. These pulse lengths correspond to bandwidths of 57.0 ppm (2.95 kHz) and 22.2 ppm (1.15 kHz) for HS and HS-EX pulses, respectively.

As mentioned above, proton decoupling was provided by the body coil and executed in broadband mode, which uses WALTZ-4 phase cycling. Decoupling power level was set to 400 W and the decoupling frequency was set to −100 Hz from the water, which corresponds to the chemical shift of 3.9 ppm. The proton decoupling

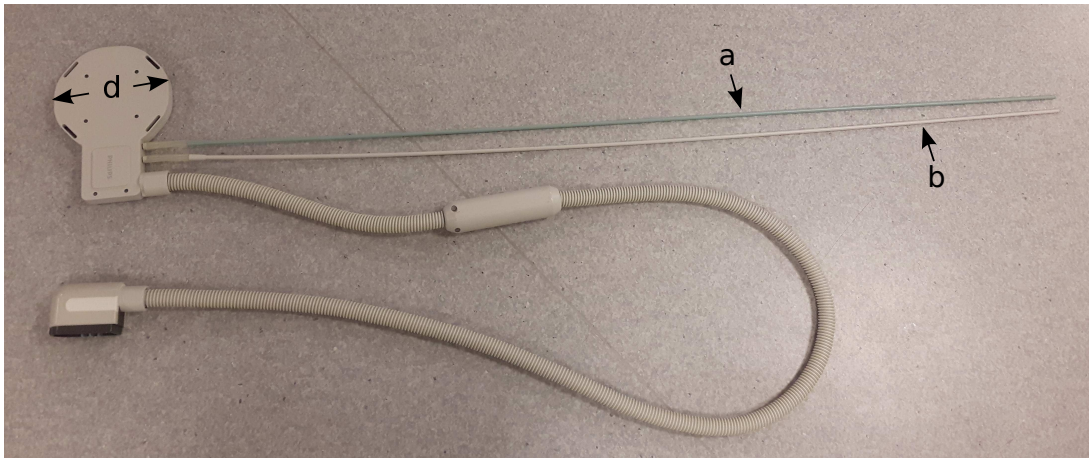

Figure 21: ^{31}P MRS loop coil was used for data acquisition. Loop diameter (d) is 14 cm. Long rods were used for tuning the frequency (a) and matching the impedance (b).

is switched on during the data acquisition time and is switched off during all other parts of the sequence as shown in Figure 4.

WALTZ-4 pulses were used for broadband irradiation prior to data acquisition period in order to improve signal gain through NOE. Duration of the irradiation also known as NOE mix time was set to 3500 ms. We used −100 Hz NOE offset frequency, similar to decoupling frequency, and NOE power level of 90 W.

Respiratory motion was controlled by instructing the subjects to adjust their breathing cycle to the pulse sequence noise, so that the excitation and pulse and data acquisition were timed to end exhalation. Respiratory triggering by using navigator belt, was not used as it would have been led to intolerable acquisition times or variable T1-weighting.

3.4.1 Shimming

Automatic pencil beam (PB) shimming was carried out using the ^{1}H body coil and the tissue water as a reference signal. In PB a number of pencil beam excitations, each one with two different echo times, are measured through the volume of interest to determine phase differences over the beams. In this process, the various orders of magnetic field gradients present in the subject are calculated and the amount of electrical current needed to correct unwanted gradients in the subject is estimated. Estimated currents are applied to the system shim and gradient coils.

In this experiment, eight shim correction components were determined: three first order (X, Y, Z) and five second order (Z^2, ZX, ZY, XY, X^2-Y^2). Second order shimming allows better homogeneity over large voxels compared to first order shimming including linear X ,Y and Z components only. Besides adjusting the shim currents, the f_0-frequency was determined from the tissue water resonance during the preparation. The total duration of this automatic procedure was approximately

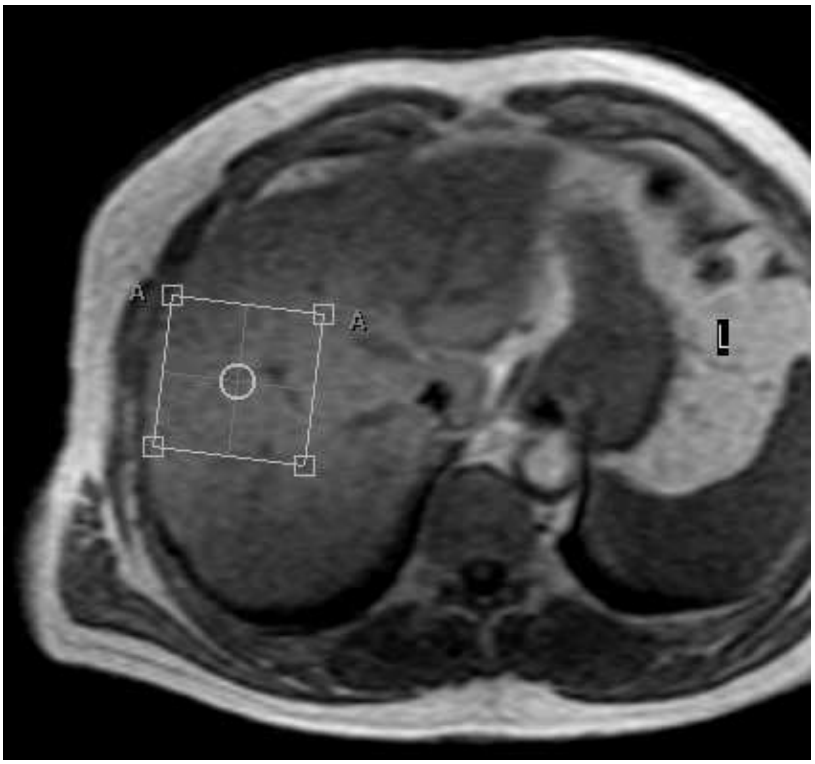

Figure 22: Transaxial localizer image showing the volume of interest placed in the the right lobe of the liver.

40 seconds.

3.4.2 Tuning and matching

The presence of patient changes the coil load and thus the characteristics of the tuned circuit. In order to optimize the performance of the measurement coil, variable capacitors were adjusted manually by means of long flexible rods (see Figure 21). The first variable capacitor was used to adjust the tuning - the frequency at which the tuned circuit resonates. This frequency equals the resonance frequency of ^{31}P at 3.0 T, approximately 51.73 MHz. To minimize the amount of reflected power, the second variable capacitor was used to adjust matching - the impedance of the loaded coil. The impedance should be 50 Ω for zero reflection.

In manual tuning mode, low power RF was swept through the resonance frequency. During tuning, reflected power was monitored as a function of frequency and had a shape of "V" (see Figure 23). The adjustment of reflected power curve was followed from the screen on the front panel of the MR imager. Curve was centred at zero frequency offset and the shape was adjusted as sharp as possible in order to achieve optimum resonance frequency and minimize the reflected power.

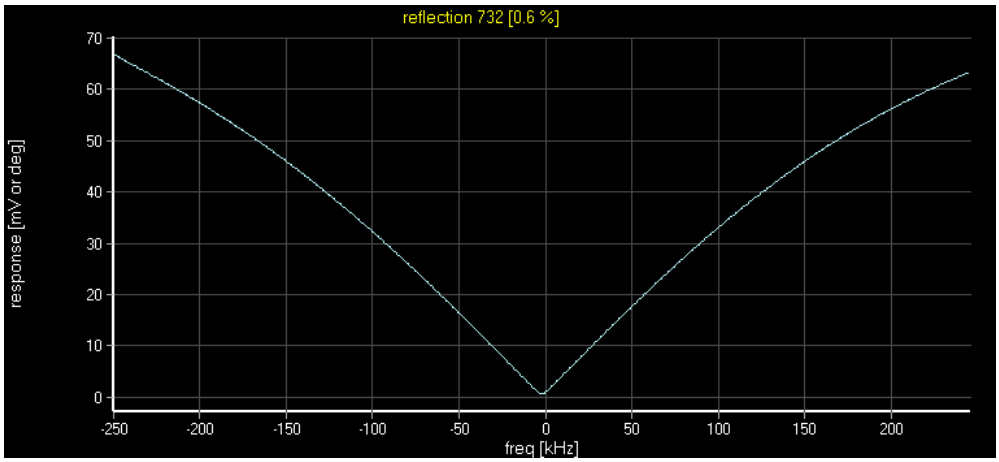

Figure 23: Capacitors were adjusted to compensate the load of the subject. Impedance was matched (vertical axis) in order to minimize reflected signal and frequency was tuned to resonance frequency of ^{31}P nuclei at 3.0T.

3.4.3 Signal processing and quantification

All spectra were preprosessed and analysed using a jMRUI v3.0 software [86]. The first two data points in time domain were removed from each FID in order to suppress wide hump in the spectra [76]. Truncated FIDs were zero filled to 4096 data points and then apodized with Gaussian function of 10 Hz for Gaussian lineshape fitting and with exponential function for Lorentzian line shape fitting. Signal intensities were assessed in time domain using AMARES algorithm (Advanced Method for Accurate, Robust and Efficient Spectral fitting) with prior knowledge [87]. Two different prior knowledge schemes were used for quantification: the first approach, widely used in literature, uses 11 Gaussian peaks and second 15 Lorentzian shaped peaks. Frequencies and line widths were picked from each spectra to be used as starting values for fitting algorithms with Gaussian and Lorentzian lineshapes. Prior knowledge was used to fix relative frequencies, line widths and signal shapes according to values presented in Tables 7 and 8. Amplitudes and relative phases were allowed to be estimated freely for each metabolite. However, overall first order phase (begin time) was fixed to 0.67 ms, which compensates the removal of the first two time points from each FID. Example of Gaussian and Lorentzian signal fitting of *in vivo* spectra is shown in Figures 24 and 25, respectively.

The peak areas or intensities and Cramér-Rao bounds (CRB) for signal fits were assessed for each metabolite. RMS noise levels were estimated from the last 100 points of the original FID. The noise was estimated as root mean squares (RMS)

$$R(x) = \sqrt{\frac{\Sigma_{k=0}^{N} x_k^2}{N}}, \tag{47}$$

where N is number of points and x_k is amplitude at point k. Noise was calculated from both 100 last points of the original FID and residue signal.

Table 7: Prior knowledge of ^{31}P metabolite peaks, frequences and line widths for Gaussian lineshape fitting scheme. Amplitudes and relative phases were estimated.

Peak	frequency	line width
PE	estimate	estimate
PC	PE–30 Hz	1.0×PE
Pi	estimate	estimate
GPE	estimate	estimate
GPC	GPE–30 Hz	1.0×GPE
PEP	0.9 ppm-2.7 ppm	1.0×GPE
γ-NTP	estimate	estimate
α-NTP	estimate	estimate
NADPH	α-NTP–40 Hz	1.0×α-NTP
UDPG	α-NTP–110 Hz	1.0×α-NTP
β-NTP	estimate	estimate

SNRs for each signal were calculated dividing the signal amplitudes by the RMS noise. Relative amplitudes were calculated dividing each intensity by the sum of all eleven intensities. Means (μ) and standard deviations (σ) were calculated for each metabolite and also for selected metabolite ratios. Moreover, coefficient of variations (c_v) were calculated by

$$c_v = \frac{\sigma}{\mu} \tag{48}$$

3.5 ^{1}H MRS acquisition and signal processing

In vivo ^{1}H MRS of the liver was performed in order to exclude subjects with excess amount fat in the liver. T1-weighted localization images were collected in transaxial plane. A $2 \times 2 \times 2$ cm^3 voxel was placed in the right liver lobe avoiding gall bladder and vascular structures. Unsuppressed ^{1}H MR spectra were obtained using PRESS localization technique with TE of 31 ms and 16 acquisitions, collecting 1024 datapoints over a 2000 Hz bandwidth. Acquisition localization images and MRS was triggered to end exhalation using navigator belt, so that the TR for MRS acquisition was $\geq$ 4000 ms.

^{1}H MRS spectra were preprocessed and analysed using a jMRUI v3.0 software. Spectra were zerofilled to 4096 data points and apodized with Gaussian and exponential filters of 5 Hz for fat and water quantification, respectively. Intensities of water and methylene resonances were quantified, and liver fat content was determined as a mass fraction as described in detail in a paper by Kotronen *et al.* [88].

Table 8: Prior knowledge of ^{31}P metabolite peaks, frequences and line widths for Lorentzian lineshape fitting scheme. Peak positions are denoted with u, d and c for upfield, downfield and center, respectively. Amplitudes and relative phases were estimated.

Peak	frequency	line width	shape
PE	estimate	estimate	Lorentzian
PC	PE–30 Hz	1.0×PE	Lorentzian
Pi	estimate	estimate	Gaussian
GPE	estimate	estimate	Lorentzian
GPC	GPE–30 Hz	1.0×GPE	Lorentzian
PEP	0.9 ppm-2.7 ppm	1.0×GPE	Lorentzian
γ-NTP (u)	estimate	estimate	Lorentzian
γ-NTP (d)	estimate	estimate	Lorentzian
α-NTP (u)	estimate	estimate	Lorentzian
α-NTP (d)	estimate	estimate	Lorentzian
NADPH	α-NTP–40 Hz	1.0×α-NTP (u)	Lorentzian
UDPG	α-NTP–110 Hz	1.0×α-NTP (d)	Lorentzian
β-NTP (u)	estimate	estimate	Lorentzian
β-NTP (c)	estimate	estimate	Lorentzian
β-NTP (d)	estimate	estimate	Lorentzian

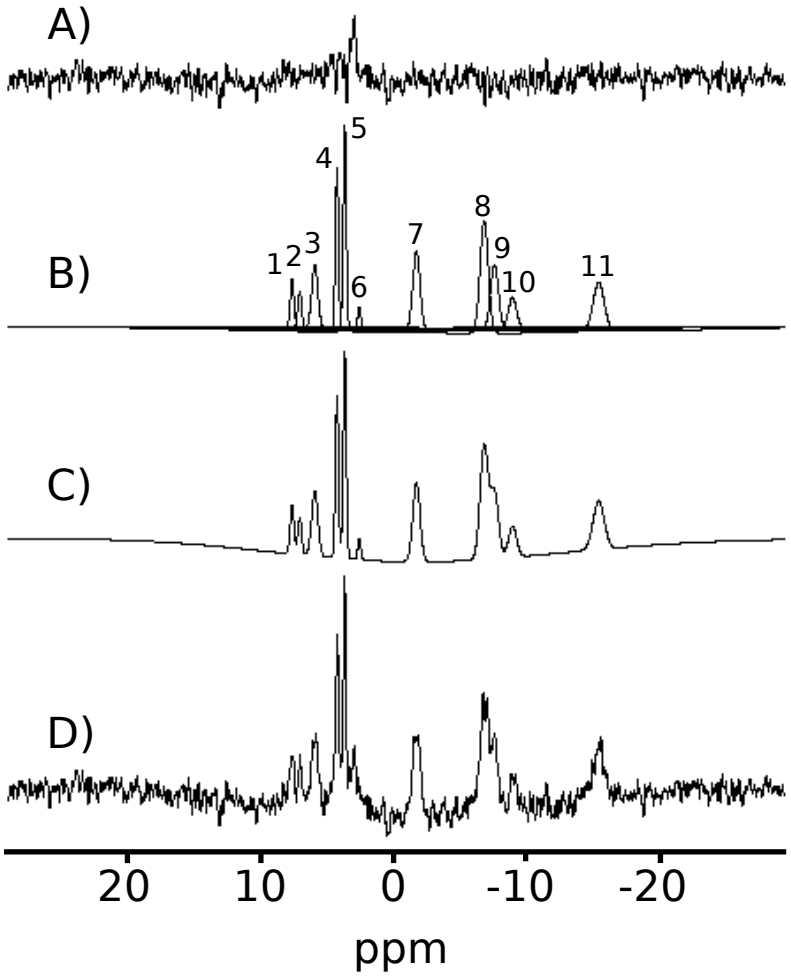

Figure 24: Signal fitting of *in vivo* spectrum with Gaussian lineshapes . A) represents residue, B) individual components of spectrum 1: PE, 2: PC 3: Pi, 4: GPE, 5: GPC, 6: PEP/PtdC, 7: γ-ATP, 8: α-ATP, 9: NADPH, 10: UDPG, 11: β-ATP, C) estimated total phosphorus singal and D) preprocessed original signal.

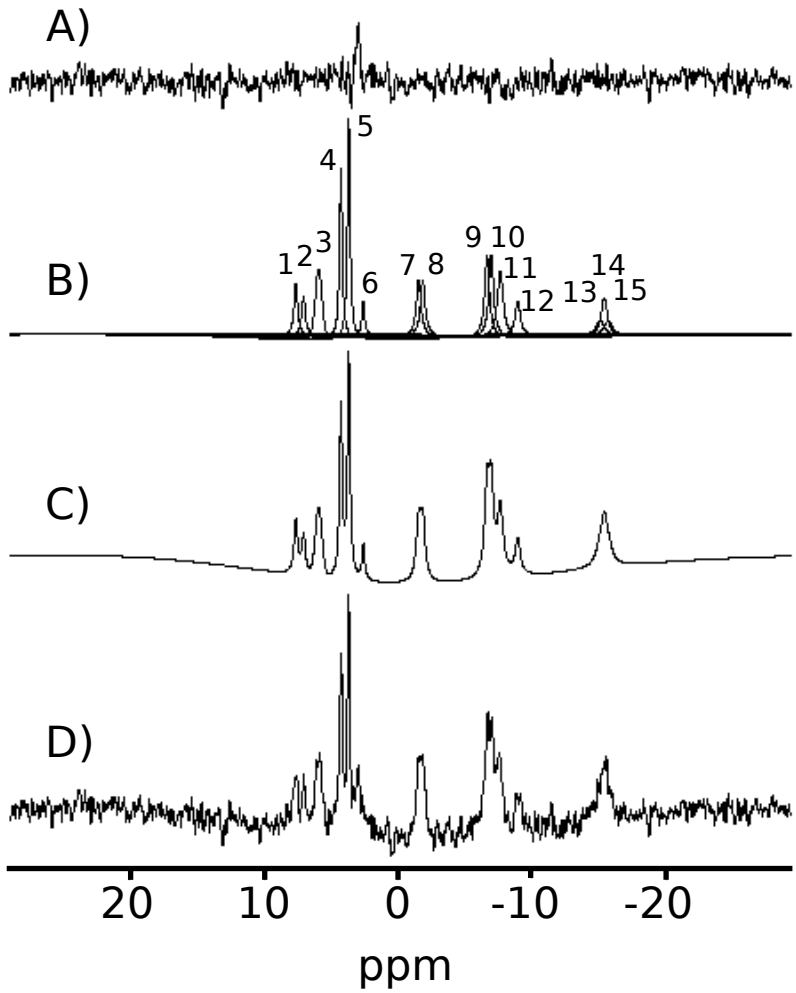

Figure 25: Signal fitting of *in vivo* spectrum with Lorentzian lineshapes . A) represents residue, B) individual components of spectrum 1: PE, 2: PC 3: Pi, 4: GPE, 5: GPC, 6: PEP/PtdC, 7-8: γ-ATP, 9-10: α-ATP, 11: NADPH, 12: UDPG, 13-15: β-ATP, C) estimated total phosphorus singal and D) preprocessed original signal.

4 Results

4.1 The effect of line broadening and noise on metabolite concentrations

For quantification, γ-ATP Lorentzian approach was very accurate when inhomogeneous component β was absent or small, but concentrations become overestimated with increasing Gaussian broadening. Gaussian fitting tends to underestimate signal concentrations independent of the magnitude of Gaussian damping factor. The dependence of quantified γ-ATP intensities on Gaussian broadening have been demonstrated with different quantification procedures in Figure 26. The effect is demonstrated on γ-ATP resonance in Figure 26, but the effect is similar for the other resonances as well. The dependence of Lorentzian lineshape fitting on Gaussian broadening can be decreased by normalizing the intensities to total phosphorus signal.

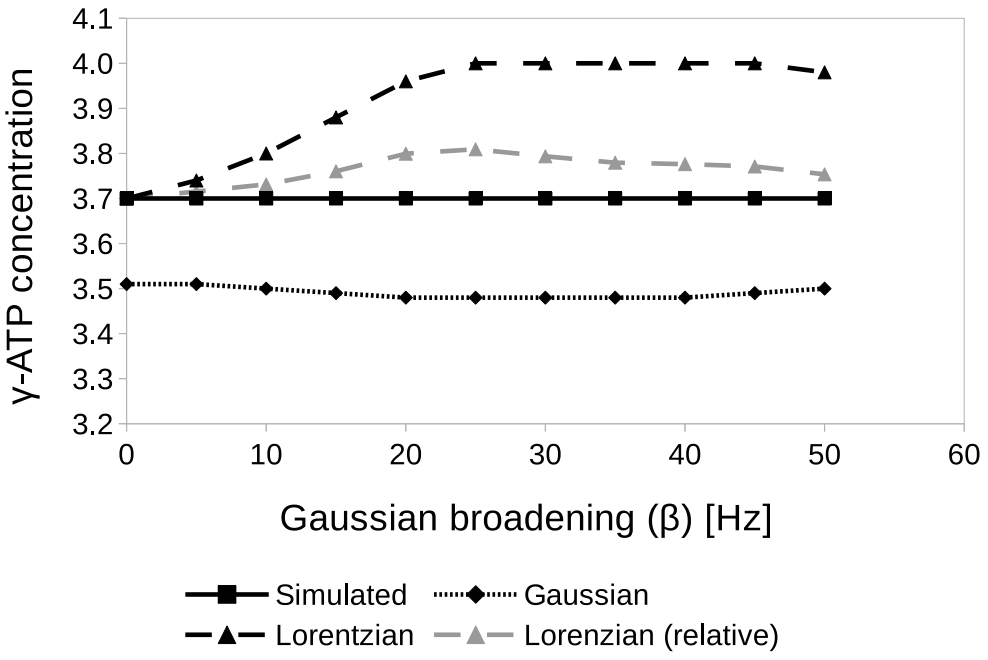

Figure 26: Concentrations of γ-ATP as a function of Gaussian broadening (β) determined by Gaussian and Lorentzian lineshape fitting from simulated spectra.

Standard deviations of the quantitated intensities increase with relative noise as is seen in Figure 27, where the dependence of quantitated intensities as a function of spectral noise level is shown for GPC. Moreover, CVs for metabolite intensities determined by Lorentzian and Gaussian lineshape fits from 20 Monte Carlo simulations with each noise level are shown in Table 10. The advantage of prior knowledge in the quantification of noisy spectra is demonstrated in Figure 28.

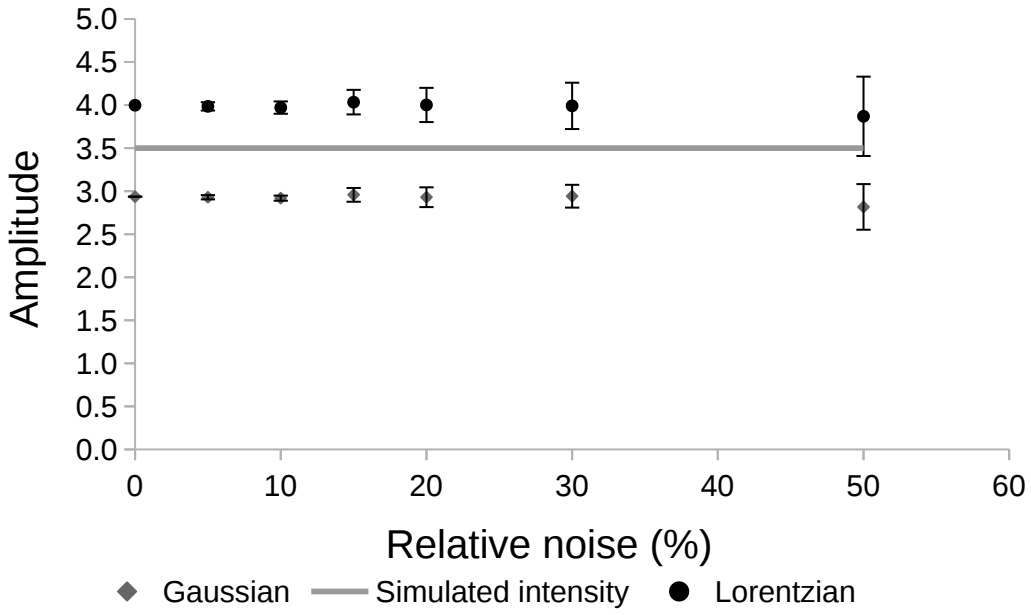

Figure 27: Concentration of simulatated glycerophosphocholine (GPC) resonance (α = 30 and α = 20) determined as a function of relative noise determined by Lorentzian and Gaussian lineshape fitting.

4.2 *In vivo* ^{31}P MRS

There were no significant differences between the noise calculated from the last points of the original FID and from the residue signal.

Signal-to-noise ratios from each study subject are presented in Table 11. Intra- and inter-individual variations for assessment of concentrations of PE, PC, Pi, GPE, GPC, PEP/PtdC, γ-NTP, α-NTP, NADPH and β-NTP, determined by Gaussian and Lorentzian lineshape fits are shown in Table 9.

4.3 *In vivo* ^{1}H MRS

Liver fat content, reported as mass fractions, was very low in all subjects with mean value of 1.0 ± 0.8 % (± SD) and range 0.3-2.6 %.

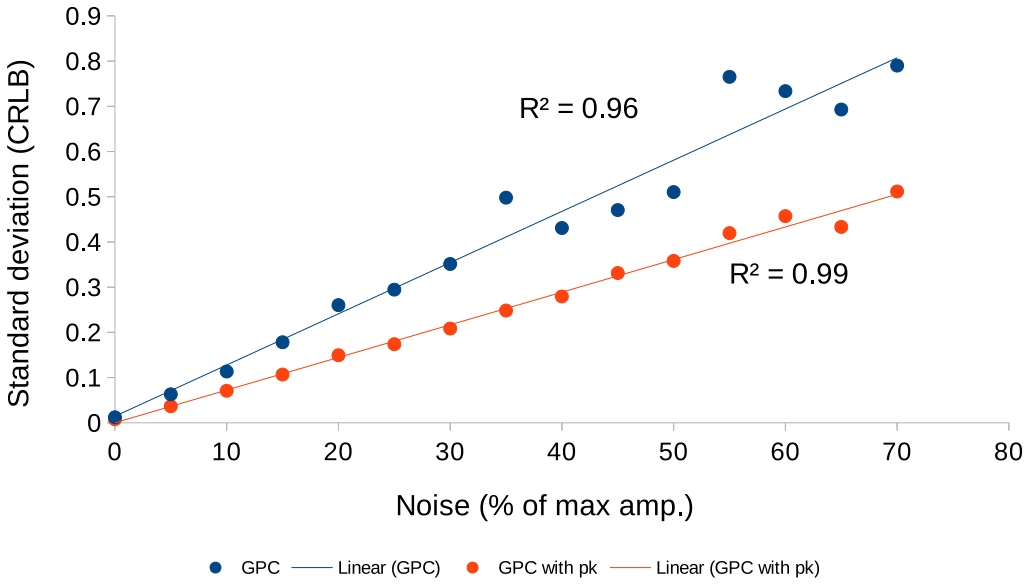

Figure 28: Dependence of standard deviation (SD) of the Lorenzian lineshape fit for glycerophosphocholine as function of relative noise. The slope is less steep (red line) when prior knowledge is utilized compared to fitting without prior knowledge (pk).

Table 9: intra- and inter-individual coefficient of variations (CV)for Gaussian and Lorenzian lineshape fits. Total phosphorus signal has been used as an internal reference. CVs are reported in percents (%).

	PE	PC	Pi	GPE	GPC	PEP	γ-NTP	α-NTP	NADPH	β-NTP
Gaussian										
intra-individual (n=3)	27	14	7	49	27	60	10	32	61	33
inter-individual (n=6)	46	31	28	29	39	52	24	38	56	67
Lorentzian										
intra-individual (n=3)	26	30	7	12	12	31	2	22	59	12
inter-individual (n=6)	41	43	16	26	29	19	10	33	24	37

Table 10: Coefficient of variations (CV) for Gaussian and Lorentzian lineshape fits of simulated spectra with varying noise levels. CVs are reported in percents (%).

Noise level (%)	5	10	15	20	30	50
fitting procedure						
Gaussian	0.8	1.0	2.7	3.9	4.5	9.4
Lorentzian	1.2	1.8	3.5	5.0	6.7	11.9

Table 11: Signal-to-noise ratios in in vivo measurements for each metabolite and subject (s1-s6).

	PE	PC	Pi	GPE	GPC	PEP	γ-NTP	α-NTP	NADPH	UDGP	β-NTP
s1	6	7	12	15	19	4	10	8	4	2	2
s2	2	4	7	6	6	2	10	14	7	4	8
s3	5	6	9	12	14	4	11	16	8	4	7
s4	6	4	12	12	15	6	14	16	11	5	10
s5	5	4	11	13	11	1	9	11	3	4	3
s6	3	2	11	11	13	3	11	18	11	5	9
mean	4	5	10	11	13	3	11	14	7	4	6
sd %	1.4	1.7	2.0	2.9	4.5	1.6	1.7	3.8	3.4	1.1	3.1

5 Discussion

Generally, Lorentzian line-fitting scheme performed better in *in vivo* spectra, producing lower CVs for both intra- and inter-individual variation as shown in Table 9.

In Lorentzian scheme, Pi, GPE, GPC, γ-NTP and β-NTP showed good repeatability with intra-individual CVs ranging from 2 - 12 %. Low CVs of Pi can be seen a bit surprising. Even though, Pi resonance is clearly distinguishable, it 1) overlaps with PME and PDE resonances (Figure 18) and 2) resonates in a frequency region that has a wide underlying resonance from motion-restricted phospholipids in cell membrane and vesicle bilayers [89]. In addition, 3) Pi is sensitive to nutritional status, since ATP (and GTP) and Pi exchange in dynamic balance [75]. Pi resonance may also have contributions from 2,3–diphophoglycerate in blood erythrocytes resonating at 3.8 ppm. On the other hand, Pi has a short T1 relaxation time and with TR of 6000 ms, resonance is not T1 weighted (TR$\geq$5T1) at 3.0 Tesla. NOE factor of Pi (Table 4) is also relatively low. Therefore, Pi is not sensitive to variation in performance of NOE. In this study, issues mentioned above were addressed by 1) using prior knowledge to minimize effect of signal overlapping, 2) truncating first times points from the FID to suppress wide baseline hump and 3) instructing subjects to fast over night to standardize nutritional status.

NTP resonances showed low intra- and relatively low inter-individual variation. γ-NTP had lowest CV for both intra- and interindividual variation. Higher CVs for α- and β- can be explained by higher chemical shift artifacts and limited bandwidths of used pulses. In addition, α-NTP suffers from overlapping of diphosphodiesters and β-NTP has a lower SNR due to tripled structure. The effect of chemical shift artifacts and pulse imperfections are expected to be greater in β-NTP compared to α-NTP.

Our study population was weighted, since there was only one male in comparison to five female subjects. However, according to my knowledge, no inter-gender differences on appearence of *in vivo* hepatic ^{31}P MR spectra has been reported.

In vivo measurements were performed on low number of subjects. Therefore, this study should be considered as a demonstrative pilot study.

Possible error sources are described in detail in following sections.

5.1 Discrepancy between simulated and *in vivo* spectra

Simulated spectra are ideal in many ways. Situation is much more complex *in vivo*, and were not disturbing in simulations. Broad resonance arising from phospholipids [76] was not modelled in these simulations, since it was suppressed in postprocessing of *in vivo* spectra by removing first two points in time domain. Incomplete suppression may still add uncertainty to the quantification of some signals, PDE, Pi and PEP/PtdC especially.

Each resonance of the spectra were modelled to be of similar linewidth (α and β). This is a rough approximation and not true for *in vivo* spectra. Metabolites in ^{31}P MR spectrum of the liver differ in size and molecular shape. Therefore, there

are variation in spectral linewidths of the metabolites, because of the variation in magnitude and form of relaxation mechanisms effecting on different metabolites.

Due to limited sensitivity, hepatic ^{31}P MR spectra are averaged from several acquisitions; 128 acquisitions in this thesis. Uncorrected phase distortion before averaging may lead to underestimation of metabolite intensities. Therefore, data should be accquired as a "time series", in which each phase cycle (8 acquisitions for ISIS sequence) is saved as a single frame allowing manual phase correction prior to signal averaging. However, poor SNR of a single frame can make phase correction challenging.

β-ATP concentrations appear to be smaller in *in vivo* experiment (Figure 18) compared to simulated resonances taken from the literature. The possible reason may be as follows: β-ATP resonating far right to the downfield at -16.26 ppm may suffer from large chemical shift artifact and limited bandwidths of pulses.

In phosphomonoester region of the hepatic ^{31}P MR spectra, PE and PC resonances overlap with several other PME resonances leading to poorer spectral resolution in this spectral region. Also, 2,3–diphophoglycerate contamination from blood may affect to Pi and PC as discussed later in detail.

5.2 Effects of imperfect localization

ISIS sequence is prone to process known as 'T1 smearing', an important source of background contamination. 'T1 smearing' arises when a non-perfect 90° excitation pulse is used in combination of with short TR ($\leq$5T1). The magnitude of this contamination depends on excitation pulse angle, inhomogeneous $B1$ field, TR/T1 ratio and ISIS experiment order [91]. This causes background contamination via imperfect cancellation of the signals outside the volume of interest.

In order to avoid T1 smearing, one of the 48 optimal experiment orders out of the 40 320 possible permutations was used. By using optimal experiment order T1 smearing can occur in only one (out of three) of the selected slices. In addition, frequency modulated 90° adiabatic hyperbolic secant pulse was used in order to achieve 90° excitation. However, non-perfect 90° flip angles might still occur due to practical implementation of the pulse.

In phantom measurements with nominal voxel size of $50 \times 50 \times 50$ mm^3 and fully relaxed conditions (TR$\geq$5T1), contamination of approximately 10-20 % has been reported [56]. In clinically feasible conditions ($TR \approx T1$), background contamination has been reported to increase from approximately 20 % to over 50 % [56].

By decreasing the voxel size relative background contamination increases. Therefore use of larger voxel, even if it extends beyond the edges of the tissue is of interest is recommended [56].

5.3 Signal contamination from non-hepatic tissues

Liver is an organ consisting of not only hepatic cells, but also other tissue types. Also, liver is prone to cardiac and respiratory motion. Therefore, it is practically

impossible to measure pure liver parenchyma (i.e. hepatic cells) by *in vivo* MRS, which has limited spatial resolution *per se*.

Hepatic vasculature structures have been reported to be up to 25 % of the total liver volume [92]. Thus, it is likely that 2,3–diphophoglycerate (2,3–DPG) resonating from blood erythrocytes will affect to the hepatic ^{31}P MR spectra. At the pH of blood, 2,3–DPG peaks resonate at 3.8 and 2.8 ppm. It is likely that signals from blood 2,3–DPG contribute to the PC and Pi and also total phosphorus signal. Li *et al* estimated from expected structural volumes and metabolite concentrations that, in theory, erythrocyte 2,3–DPG could account for up to 45 % of PC and 18 % of Pi signals, when relaxation effects are neglected. Signal contamination from blood erythrocytes hamper reproducibility (especially inter-individual) of PE and Pi and also indirectly all metabolites when total phosphorus signal is used as an internal reference. Blood supply to the liver is increased by exhalation, bed rest and digestion of food, while standing position and physical exercise will do the opposite. Besides, effective blood supply, liver can store approximately 300 mL of blood. As a consequence of a cardiac dysfunction, liver can double its blood storage [93].

The small resonance at 2.06 ppm, upfield side of GPC is not always clearly differentiable. Conventionally, this resonance has been assigned to PEP [77, 78], or extraction and perchlhoric acid artifacts in *in vitro* studies [94, 71]. PEP is involved in both glycolysis and gluconeogenesis. The conversion of PEP to ADP by puryvate kinase generates one molecule of ATP. In metabolic studies, MRS experiments are typically performed after a night or several hours of fasting, when increase of PEP through gluconeosis could be expected. However, reversed phosphorylation of puryvate to PEP through phosphoenolpuryvate-carboxykinase is considered to be a rate-limiting step in gluconeogenesis and thus PEP concentrations are expected to be relatively small [79].

Several *in vitro* and *in vivo* studies have shown a dominant peak of phosphatidylcholine (PtdC), a typical phosphodiester and part of bile lecithin, resonating at the same position with PEP. Since voxel size in single voxel ^{31}P MRS is relatively large, signal contamination from the intrahepatic bile ducts cannot be avoided, but the voxel has to be placed carefully to avoid contamination from the gall bladder, where bile is approximately 5 times more concentrated. Also, triggering of respiratory motion is crucial to avoid contamination from the gall bladder. If contamination occurs, it can directly hamper the quantification of neighbouring GPC at the downfield side and indirectly all metabolites if total phosphorus signal is used as an internal reference. PtdC protects bile ducts from the harmful bile acids [95]. An *in vitro* NMR study of human bile has shown conversion PtdC to GPC in patients with primary sclerosing cholangitis and thus quantitation of PtdC in the liver and gall bladder may have diagnostic value in the future [96].

Occasionally a small resonance peak can be seen at 0.0 ppm. Phosphocreatine PCr is a dominant peak in ^{31}P muscle spectrum and thus it's used as a zero reference for ppm scale. It has been suggested that PCr is present in small quantities in human liver [85], but typically it has been considered as a marker of extra-hepatic muscle contamination [90].

5.4 Effect of physiological state and diat on metabolite levels

In a recent study, Hakkarainen *et al.* [75] found decrease of liver NTP after 60 min exercise session combined with delayed impact of fat intake from standardized fat rich meal. Both intervention mimiced normal behaviour underlining the importance standardizing the physiological state prior to hepatic ^{31}P MRS experiment. Further, this observation was linked to fueling of gluconeogenesis by ATP and GTP, supported by various blood samples drawn during the experiment. Since ATP and Pi exchange in dynamic balance, variations in physiological state may increase variations in Pi and its, partly overlapping, resonances of PC and GPE at downfield and upfield sides, respectively.

Abdelmalek *et al.* [75] reported reduced ATP content in obese type 2 diabetes mellitus (T2DM) patients with increased habitual diatery fructose consumption compared to corresponding patients with minimal fructose intake. This study was performed on patients with T2DM, but it shows large habitual variation in food intake may increase variation in metabolite levels.

Increased omega 3 fatty acid intake has been shown to effect hepatic ^{31}P MR spectra of humans. Dagnelie *et al.* [94] reported a significant increase in PDE to ATP ratios after 1 and 3 days of 50 mL supplementary fish oil intake (12 g omega 3 fatty acids) compared to baseline measurement. Their *in vitro* ^{31}P MR spectra on rat liver extracts further suggested that GPC and possibly GPE were responsible for rising PDE levels. Also, PC levels were reduced in rat liver after intake of supplementary fish oil.

5.5 Effects related to measurement parameters

Since ISIS is a FID–based localization technique, metabolites are free from T2 weighting. However, relatively large variation in T1 relaxation times of different metabolites have been reported. Not only between different studies (Table 12), but also between subjects inside the same study [39]. Incorporating a T1 measurement into a study protocol, would require a 4–5 spectral acquisitions with varying inversion recovery times. This would increase the measurement duration approximately by an hour, which is not feasible in clinical environment. On the other hand, T1 times of almost 10 seconds have been reported for GPE [39] at B_0 of 3.0T and, thus, increasing the TR in order to eliminate T1-weighting, would also lead infeasible acquisition times. Therefore, some T1–weighting needs to tolerated in practice. This is present for PDE and also PME resonance with long spin lattice relaxation times, whereas Pi and NTP resonances with T1 relaxation times less than 1 second do not suffer from T1-weighting directly. However, when a total phosphorus signal is used as an internal reference, incomplete recovery of PDE (and PME) will indirectly affect to quantification of these metabolites with short T1 as well. Utilization of NOE, makes quantification more complex. Contribution of NOE is unique for each metabolite as shown in Table 4 and depended from environment of metabolites and external field strenght B_0. Therefore, utilization of NOE hampers reliability of

aquous solutions as an external concentration reference.

5.6 Field strenght considerations

Generally, MR spectroscopy is one of the biggest winners of the higher field strenghts. Greater energy difference between spin states leads to improved SNR, which often crucial for nuclei other than proton, as these usually are low in concentration (compared to conventional MRI) and have limited sensitivity (Table 1). In theory, SNR increases linearly with magnetic field strength as the square of the field strength. However, situation is more complex in real life. As Larmor frequency increases linearly with the field strength according to equation 2, radio-frequency penetration decreases and T1 relaxation times increase. While B_0 increases, CSA becomes increasingly important relaxation mechanism. Whereas the frequency range increases according to B_0, the line widths increase linearly with B_0^2, limiting the benefits of increased field strength. Also, as relative effects of dipole-dipole interactions decrease, utility of NOE in boosting SNR decreases. Recently, Chmelik *et al.* managed to separate PDE and PME into their subcomponents in hepatic ^{31}P MR spectra at 7.0T with great success without utilizing proton-decoupling [97]. They also observed that T1 relaxation times of both PME and PDE resonances increased significantly at 7.0T compared to 3.0T. However, this was not true for Pi and ATP resonances. Based on this observation they concluded that dipolar interactions prevail as a dominant relaxation mechanism over CSA for PDE and PME. Therefore, proton-decoupling could further improve spectral resolution and NOE SNR in hepatic ^{31}P MRS at 7.0T.

5.7 In summary

This thesis shows that to carry out succesful ^{31}P MR spectroscopy analysis, several issues have to be considered:

- Lorenzian lineshape fit is sensitive to inhomogeneaus broadening and overestimates signal intensities with Gaussian broadening.
- Gaussian lineshape fit underestimates signal intensities, but is not sensitive for inhomogeneaous broadening.
- Dependence of Lorenzian lineshape fit on inhogeneous broadening can be decreased by using the total phosphorus signal as an internal reference.
- Lineshape fitting is insensitive to noise.
- Lorenzian lineshape scheme performed better on *in vivo* spectra.

In order to to avoid signal contamination from vascular structures and gall bladder, attention has to be paid to careful voxel placement, and use of respiratory triggering if possible. Using long TR minimizes T1-weighting in signal intensities. Physiologigal state of the study subjects has to be standardized by instructing to avoid heavy exercise prior to MR experiment and standardizing meal intake.

Table 12: Hepatic *In Vivo* T1-values from literature

Study	B_0	PE	PC	PME	Pi	GPE	GPC	PEP	PDE	γ-NTP	α-NTP	NADPH	β-NTP
Schmid *et al.* [39]	3.0T	1.81	2.24		0.73	6.98	4.26			0.43	0.58		0.55
Buchli *et al.* [90]	1.5T			1.6	0.8				1.9	0.5	0.9		0.5
Wylezinska *et al.* [50]	1.5T			2.76					4.37				
Wylezinska *et al.* [50]	3.0T			2.80					4.92				
Li *et al.* [59]	1.5T	2.2	2.3	2.1	0.8	5.6	6.6	2.0	6.1	0.4	0.6	2.6	0.4

References

[1] F. Bloch, "Nuclear induction," *Physical Review*, vol. 70, no. 7-8, p. 460, 1946.

[2] N. Bloembergen, E. M. Purcell, and R. V. Pound, "Relaxation effects in nuclear magnetic resonance absorption," *Physical Review*, vol. 73, no. 7, pp. 679–712, 1948.

[3] W. G. Proctor and F. C. Yu, "The dependence of a nuclear magnetic resonance frequency upon chemical compound," *Physical Review*, vol. 77, no. 5, pp. 717–717, 1950.

[4] R. R. Ernst and W. A. Anderson, "Application of fourier transform spectroscopy to magnetic resonance," *Review of Scientific Instruments*, vol. 37, no. 1, pp. 93–102, 1966.

[5] P. Rinck. (2014) Europe celebrates the forgotten pioneer of MRI: Dr. Erik Odeblad. Column in AuntMinnieEurope.com. Cited 25.8.2017. [Online]. Available: http://www.auntminnieeurope.com/index.aspx?sec=ser&sub=def&pag=dis&ItemID=606754&wf=1501

[6] E. Odeblad and G. Lindström, "Some preliminary observations on the proton magnetic resonance in biologic samples," *Acta Radiologica*, vol. 43, no. suppl 434, pp. 469–476, 1955.

[7] R. Damadian, "Tumor detection by nuclear magnetic resonance," *Science*, vol. 171, no. 3976, pp. 1151–1153, 1971.

[8] R. Damadian, "Apparatus and method for detecting cancer in tissue," U.S. Patent 3,789,832, February 5, 1974.

[9] P. C. Lauterbur, "Image formation by induced local interactions: Examples employing nuclear magnetic resonance," *Nature*, vol. 242, no. 5394, pp. 190–191, 1973.

[10] P. K. Grannell and P. Mansfield, "NMR 'diffraction' in solids?" *Journal of Physics C: Solid State Physics*, vol. 6, no. 22, p. L422, 1973.

[11] A. N. Garroway, P. K. Grannell, and P. Mansfield, "Image formation in NMR by a selective irradiative process," *Journal of Physics C: Solid State Physics*, vol. 7, no. 24, p. L457, 1974.

[12] R. B. Moon and J. H. Richards, "Determination of intracellular pH by ^{31}P magnetic resonance," *Journal of Biological Chemistry*, vol. 248, no. 20, pp. 7276–7278, 1973.

[13] D. I. Hoult, S. J. W. Busby, D. G. Gadian, G. K. Radda, R. E. Richards, and P. J. Seeley, "Observation of tissue metabolites using ^{31}P nuclear magnetic resonance," *Nature*, vol. 252, no. 5481, pp. 285–287, 1974.

[14] B. Chance, Y. Nakase, M. Bond, J. S. Leigh, and G. McDonald, "Detection of ^{31}P nuclear magnetic resonance signals in brain by in vivo and freeze-trapped assays," *Proceedings of the National Academy of Sciences*, vol. 75, no. 10, pp. 4925–4929, 1978.

[15] R. E. Gordon, P. E. Hanley, D. Shaw, D. G. Gadian, G. K. Radda, P. Styles, P. J. Bore, and L. Chan, "Localization of metabolites in animals using ^{31}P topical magnetic resonance," *Nature*, vol. 287, no. 5784, pp. 736–738, 1980.

[16] J. J. H. Ackerman, T. H. Grove, G. G. Wong, D. G. Gadian, and G. K. Radda, "Mapping of metabolites in whole animals by ^{31}P NMR using surface coils," *Nature*, vol. 283, no. 5743, pp. 167–170, 1980.

[17] R. Oberhaensli, G. Galloway, D. Taylor, P. Bore, and G. Radda, "Assessment of human liver metabolism by phosphorus-31 magnetic resonance spectroscopy," *The British Journal of Radiology*, vol. 59, no. 703, pp. 695–699, 1986.

[18] P. Styles, C. A. Scott, and G. K. Radda, "A method for localizing high-resolution NMR spectra from human subjects," *Magnetic Resonance in Medicine*, vol. 2, no. 4, pp. 402–409, 1985.

[19] P. R. Luyten, G. Bruntink, F. M. Sloff, J. W. Vermeulen, J. I. van der Heijden, J. A. den Hollander, and A. Heerschap, "Broadband proton decoupling in human ^{31}P NMR spectroscopy," *NMR in Biomedicine*, vol. 1, no. 4, pp. 177–183, 1989.

[20] P. Thampanitchawong and T. Piratvisuth, "Liver biopsy: complications and risk factors," *World Journal of Gastroenterology*, vol. 5, no. 4, pp. 301–304, 1999.

[21] V. Ratziu, F. Charlotte, A. Heurtier, S. Gombert, P. Giral, E. Bruckert, A. Grimaldi, F. Capron, and T. Poynard, "Sampling variability of liver biopsy in nonalcoholic fatty liver disease," *Gastroenterology*, vol. 128, no. 7, pp. 1898–1906, 2005.

[22] A. Regev, M. Berho, L. J. Jeffers, C. Milikowski, E. G. Molina, N. T. Pyrsopoulos, Z.-Z. Feng, K. R. Reddy, and E. R. Schiff, "Sampling error and intraobserver variation in liver biopsy in patients with chronic HCV infection," *The American Journal of Gastroenterology*, vol. 97, no. 10, pp. 2614–2618, 2002.

[23] L. S. Szczepaniak, P. Nurenberg, D. Leonard, J. D. Browning, J. S. Reingold, S. Grundy, H. H. Hobbs, and R. L. Dobbins, "Magnetic resonance spectroscopy to measure hepatic triglyceride content: prevalence of hepatic steatosis in the general population," *AJP - Endocrinology and Metabolism*, vol. 288, no. 2, pp. E462–468, 2005.

[24] J. Ruiz-Cabello, B. P. Barnett, P. A. Bottomley, and J. W. Bulte, "Fluorine (19F) MRS and MRI in biomedicine," *NMR in Biomedicine*, vol. 24, no. 2, pp. 114–129, 2011.

[25] N. Beckmann, R. Fried, I. Turkalj, J. Seeling, U. Keller, and G. Stalder, "Non-invaive observation of hepatic glycogen formation in man by 13C MRS after oral and intravenous glucose administration," *Magnetic Resonance in Medicine*, vol. 29, no. 5, pp. 583–590, 1993.

[26] Q.-B. Wang, H. Zhu, H.-L. Liu, and B. Zhang, "Performance of magnetic resonance elastography and diffusion-weighted imaging for the staging of hepatic fibrosis: A meta-analysis," *Hepatology*, vol. 56, no. 1, pp. 239–247, 2012.

[27] R. Bülow, B. Mensel, P. Meffert, D. Hernando, M. Evert, and J.-P. Kühn, "Diffusion-weighted magnetic resonance imaging for staging liver fibrosis is less reliable in the presence of fat and iron," *European Radiology*, vol. 23, no. 5, pp. 1281–1287, 2013.

[28] Y. Boulanger, M. Amara, L. Lepanto, G. Beaudoin, B. N. Nguyen, G. Allaire, M. Poliquin, and V. Nicolet, "Diffusion-weighted MR imaging of the liver of hepatitis C patients," *NMR in Biomedicine*, vol. 16, no. 3, pp. 132–136, 2003.

[29] M. Friedrich-Rust, M.-F. Ong, S. Martens, C. Sarrazin, J. Bojunga, S. Zeuzem, and E. Herrmann, "Performance of transient elastography for the staging of liver fibrosis: A meta-analysis," *Gastroenterology*, vol. 134, no. 4, pp. 960–974.e8, 2008.

[30] S. Singh, S. K. Venkatesh, R. Loomba, Z. Wang, C. Sirlin, J. Chen, M. Yin, F. H. Miller, R. N. Low, T. Hassanein, E. M. Godfrey, P. Asbach, M. H. Murad, D. J. Lomas, J. A. Talwalkar, and R. L. Ehman, "Magnetic resonance elastography for staging liver fibrosis in non-alcoholic fatty liver disease: a diagnostic accuracy systematic review and individual participant data pooled analysis," *European Radiology*, vol. 26, no. 5, pp. 1431–1440, 2016.

[31] B. Noren, O. Dahlqvist, P. Lundberg, S. Almer, S. Kechagias, M. Ekstedt, L. Franzen, S. Wirell, and O. Smedby, "Separation of advanced from mild fibrosis in diffuse liver disease using ^{31}P magnetic resonance spectroscopy," *European Journal of Radiology*, vol. 66, no. 2, pp. 313–320, 2008.

[32] A. K. P. Lim, N. Patel, G. Hamilton, J. V. Hajnal, R. D. Goldin, and S. D. Taylor-Robinson, "The relationship of in vivo ^{31}P MR spectroscopy to histology in chronic hepatitis C," *Hepatology*, vol. 37, no. 4, pp. 788–794, 2003.

[33] A. Hakkarainen, L. Puustinen, R. Kivisaari, S. Boyd, U. Nieminen, P. Arkkila, and N. Lundbom, "Metabolic profile of liver damage in non-cirrhotic virus C and autoimmune hepatitis: A proton decoupled ^{31}P-MRS study," *European Journal of Radiology*, vol. 90, pp. 205–211, 2017.

[34] E. Godfrey, A. Patterson, A. Priest, S. Davies, I. Joubert, A. Krishnan, N. Griffin, A. Shaw, G. Alexander, M. Allison, W. H. Griffiths, A. S. Gimson, and D. Lomas, "A comparison of MR elastography and ^{31}P MR spectroscopy with histological staging of liver fibrosis," *European Radiology*, vol. 22, no. 12, pp. 2790–2797, 2012.

[35] S. Nair, V. P. Chacko, C. Arnold, and A. M. Diehl, "Hepatic ATP reserve and efficiency of replenishing: Comparison between obese and nonobese normal individuals," *The American Journal of Gastroenterology*, vol. 98, no. 2, pp. 466–470, 2003.

[36] S. F. Solga, A. Horska, S. Hemker, S. Crawford, C. Diggs, A. M. Diehl, F. L. Brancati, and J. M. Clark, "Hepatic fat and adenosine triphosphate measurement in overweight and obese adults using ^{1}H and ^{31}P magnetic resonance spectroscopy," *Liver International*, vol. 28, no. 5, pp. 675–681, 2008.

[37] J. Szendroedi, M. Chmelik, A. I. Schmid, P. Nowotny, A. Brehm, M. Krssak, E. Moser, and M. Roden, "Abnormal hepatic energy homeostasis in type 2 diabetes," *Hepatology*, vol. 50, no. 4, pp. 1079–1086, 2009.

[38] M. Dezortova, P. Taimr, A. Skoch, J. Spicak, and M. Hajek, "Etiology and functional status of liver cirrhosis by ^{31}P MR spectroscopy," *World Journal of Gastroenterology*, vol. 11, no. 44, pp. 6926–6931, 2005.

[39] A. I. Schmid, M. Chmelik, J. Szendroedi, M. Krssak, A. Brehm, E. Moser, and M. Roden, "Quantitative ATP synthesis in human liver measured by localized ^{31}P spectroscopy using the magnetization transfer experiment," *NMR in Biomedicine*, vol. 21, no. 5, pp. 437–443, 2008.

[40] A. I. Schmid, J. Szendroedi, M. Chmelik, M. Krssák, E. Moser, and M. Roden, "Liver ATP synthesis is lower and relates to insulin sensitivity in patients with type 2 diabetes," *Diabetes Care*, vol. 34, no. 2, pp. 448–453, 2011.

[41] M. H. Levitt, *Spin Dynamics: Basics of Nuclear Magnetic Resonance*, 2nd ed. Hoboken, United States: John Wiley & Sons Ltd, 2008.

[42] P. S. Tofts, Ed., *Quantitative MRI of the Brain: Measuring Changes Caused by Disease*. England: John Wiley & Sons Ltd, 2004.

[43] R. A. de Graaf, *Spin Dynamics: Basics of Nuclear Magnetic Resonance*, 2nd ed. England: John Wiley & Sons Ltd, 2007.

[44] D. E. Leyden and R. H. Cox, Eds., *Analytical application of NMR*, ser. Chemical analysis - a series of monographs on analytical chemistry and its applications. United States: John Wiley & Sons Ltd, 1977, vol. 48.

[45] P. A. Boulby and F. J. Rugg-Gunn, *T2: The Transverse Relaxation Time*, ser. Quantitative MRI of the Brain. John Wiley & Sons, Ltd, 2004, pp. 143–201.

[46] I. Solomon, "Relaxation processes in a system of two spins," *Physical Review*, vol. 99, no. 2, p. 559, 1955.

[47] E. R. Andrew and R. Gaspar, "Mechanisms of ^{31}P relaxation in phosphorus metabolites," *Magnetic Resonance Materials in Physics, Biology and Medicine*, vol. 2, no. 3, pp. 421–423, 1994.

[48] R. A. de Graaf, *In Vivo NMR Spectroscopy: Dynamic Aspects*, ser. In Vivo NMR Spectroscopy. John Wiley & Sons, Ltd, 2007, pp. 111–190.

[49] T. E. Bates, S. R. Williams, and D. G. Gadian, "Phosphodiesters in the liver: The effect of field strength on the ^{31}P signal," *Magnetic Resonance in Medicine*, vol. 12, no. 1, pp. 145–150, 1989.

[50] M. Wylezinska, J. F. L. Cobbold, J. Fitzpatrick, M. J. W. McPhail, M. M. E. Crossey, H. C. Thomas, J. V. Hajnal, W. Vennart, I. J. Cox, and S. D. Taylor-Robinson, "A comparison of single-voxel clinical in vivo hepatic ^{31}P MR spectra acquired at 1.5 and 3.0 Tesla in health and diseased states," *NMR in Biomedicine*, vol. 24, no. 3, pp. 231–237, 2011.

[51] A. Räisänen and A. Lehto, *Radiotekniikan perusteet*. Helsinki: Oy Yliopistokustannus/Otatieto, 2001.

[52] P. A. Bottomley, "Spatial localization in nmr spectroscopy in vivo," *Annals of the New York Academy of Sciences*, vol. 508, pp. 333–348, 1987.

[53] P. A. Bottomley, "Selective volume method for performing localized NMR spectroscopy," U.S. Patent 4,480,228, October 30, 1984.

[54] J. Frahm, K.-D. Merboldt, and W. Hanicke, "Localized proton spectroscopy using stimulated echoes," *Journal of Magnetic Resonance (1969)*, vol. 72, no. 3, pp. 502–508, 1987.

[55] R. J. Ordidge, A. Connelly, and J. A. B. Lohman, "Image-selected in vivo spectroscopy (ISIS). A new technique for spatially selective NMR spectroscopy," *Journal of Magnetic Resonance (1969)*, vol. 66, no. 2, pp. 283–294, 1986.

[56] S. F. Keevil, "Spatial localization in nuclear magnetic resonance spectroscopy," *Physics in Medicine and Biology*, vol. 51, no. 16, pp. R579–R636, 2006.

[57] R. A. de Graaf, *Basic Principles*, ser. In Vivo NMR Spectroscopy; NMR Spectroscopy. John Wiley & Sons, Ltd, 2007, pp. 1–42.

[58] M. Timonen, L. Kankaanranta, N. Lundbom, J. Collan, A. Kangasmäki, M. Kortesniemi, A. M. Häkkinen, A. Lönngren, S. Karjalainen, M. Rasilainen, J. Leinonen, T. Huitti, J. Jääskeläinen, M. Kouri, S. Savolainen, and S. Heikkinen, "^{1}H MRS studies in the Finnish boron neutron capture therapy project: Detection of 10B-carrier, l-p-boronophenylalanine-fructose," *European Journal of Radiology*, vol. 56, no. 2, pp. 154–159, 2005.

[59] C. Li, W. Negendank, J. Murphy-Boesch, K. Padavic-Shaller, and T. Brown, "Molar quantitation of hepatic metabolites in vivo in proton-decoupled, nuclear overhauser effect enhanced ^{31}P NMR spectra localized by three-dimensional chemical shift imaging," *NMR in Biomedicine*, vol. 9, no. 4, pp. 141–155, 1996.

[60] J. Cooley and J. Tukey, "An algorithm for the machine calculation of complex fourier series," *Mathematics of Computation*, vol. 19, no. 90, pp. 297–301, 1965.

[61] S. Cavassila, S. Deval, C. Huegen, D. van Ormondt, and D. Graveron-Demilly, "Cramér-rao bounds: an evaluation tool for quantitation," *NMR in Biomedicine*, vol. 14, no. 4, pp. 278–283, 2001.

[62] (2017) Encyclopædia britannica website. Cited 29.8.2017. [Online]. Available: https://www.britannica.com/science/liver

[63] Z. Kmiec, "Cooperation of liver cells in health and disease," *Advances in Anatomy, Embryology, and Cell Biology*, vol. 161, pp. III–XIII, 1–151, 2001.

[64] (2016) Biliary tract webpage on Wikipedia. Cited 26.4.2017. [Online]. Available: https://en.wikipedia.org/wiki/Biliary_tract

[65] W. W. Lautt and C. V. Greenway, "Conceptual review of the hepatic vascular bed," *Hepatology*, vol. 7, no. 5, pp. 952–963, 1987.

[66] V. Capitan, J.-M. Petit, S. Aho, P.-H. Lefevre, S. Favelier, R. Loffroy, P. Hillon, D. Krausé, J.-P. Cercueil, and B. Guiu, "Macroscopic heterogeneity of liver fat: an MR-based study in type-2 diabetic patients," *European Radiology*, vol. 22, no. 10, pp. 2161–2168, 2012.

[67] R. de Graaf, *In Vivo NMR Spectroscopy: Principles and Techniques*. Wiley, 1998.

[68] W.-I. Jung, S. Widmaier, U. Seeger, M. Bunse, A. Staubert, L. Sieverding, K. Straubinger, F. van Erckelens, F. Schick, G. Dietze, and O. Lutz, "Phosphorus J coupling constants of ATP in human myocardium and calf muscle," *Journal of Magnetic Resonance, Series B*, vol. 110, no. 1, pp. 39–46, 1996.

[69] S. F. Solga, A. Horska, J. M. Clark, and A. M. Diehl, "Hepatic ^{31}P magnetic resonance spectroscopy: a hepatologist's user guide," *Liver International*, vol. 25, no. 3, pp. 490–500, 2005.

[70] P. J. Harvey, J. E. Gready, H. M. Hickey, D. G. L. Couteur, and A. J. McLean, "^{31}P and ^{1}H NMR spectroscopic studies of liver extracts of carbon tetrachloride-treated rats," *NMR in Biomedicine*, vol. 12, no. 6, pp. 395–401, 1999.

[71] J. D. Bell, I. J. Cox, J. Sargentoni, C. J. Peden, D. K. Menon, C. S. Foster, P. Watanapa, R. A. Iles, and J. Urenjak, "A ^{31}P and ^{1}H-NMR investigation in vitro of normal and abnormal human liver," *Biochimica et Biophysica Acta*, vol. 1225, no. 1, pp. 71–77, 1993.

[72] S. R. Goodman, Ed., *Medical Cell Biology*, 2nd ed. Philadelphia, PA, USA: Lippincott-Raven, 1998.

[73] S. D. Taylor-Robinson, J. Sargentoni, J. D. Bell, E. L. Thomas, C. D. Marcus, K. K. Changani, N. Saeed, H. J. F. Hodgson, B. R. Davidson, A. K. Burroughs, K. Rolles, C. S. Foster, and I. J. Cox, "In vivo and in vitro hepatic phosphorus-31 magnetic resonance spectroscopy and electron microscopy in chronic ductopenic rejection of human liver allografts," *Gut*, vol. 42, no. 5, pp. 735–743, 1998.

[74] E. J. Murphy, T. E. Bates, S. R. Williams, T. Watson, K. M. Brindle, B. Rajagopalan, and G. K. Radda, "Endoplasmic reticulum: the major contributor to the PDE peak in hepatic ^{31}P-NMR spectra at low magnetic field strengths," *Biochimica et Biophysica Acta (BBA) - Biomembranes*, vol. 1111, no. 1, pp. 51–58, 1992.

[75] A. Hakkarainen, J. Lundbom, E. Tuominen, M.-R. Taskinen, K. Pietilainen, and N. Lundbom, "Measuring short-term liver metabolism non-invasively: postprandial and post-exercise ^{1}H and ^{31}P MR spectroscopy," *Magnetic Resonance Materials in Physics, Biology and Medicine*, vol. 28, no. 1, pp. 57–66, 2015.

[76] G. Hamilton, N. Patel, D. M. Forton, J. V. Hajnal, and S. D. Taylor-Robinson, "Prior knowledge for time domain quantification of in vivo brain or liver ^{31}P mr spectra," *NMR in Biomedicine*, vol. 16, no. 3, pp. 168–176, 2003.

[77] R. Shulman, T. Brown, K. Ugurbil, S. Ogawa, S. Cohen, and J. den Hollander, "Cellular applications of ^{31}P and ^{13}C nuclear magnetic resonance," *Science*, vol. 205, no. 4402, pp. 160–166, 1979.

[78] K. Sevastianova, A. Hakkarainen, A. Kotronen, A. Cornér, P. Arkkila, J. Arola, J. Westerbacka, R. Bergholm, J. Lundbom, N. Lundbom, and H. Yki-Järvinen, "Nonalcoholic fatty liver disease: Detection of elevated nicotinamide adenine dinucleotide phosphate with in vivo 3.0-T ^{31}P MR spectroscopy with proton decoupling," *Radiology*, vol. 256, no. 2, pp. 466–473, 2010.

[79] R. Rognstad, "Rate-limiting steps in metabolic pathways." *Journal of Biological Chemistry*, vol. 254, no. 6, pp. 1875–1878, 1979.

[80] A. Bierwagen, P. Begovatz, P. Nowotny, D. Markgraf, B. Nowotny, C. Koliaki, G. Giani, B. Klüppelholz, J. Lundbom, and M. Roden, ""characterization of the peak at 2.06 ppm in ^{31}P magnetic resonance spectroscopy of human liver: phosphoenolpyruvate or phosphatidylcholine?"," *NMR in Biomedicine*, vol. 28, no. 7, pp. 898–905, 2015.

[81] M. Chmelik, L. Valkovic, P. Wolf, W. Bogner, M. Gajdosik, E. Halilbasic, S. Gruber, M. Trauner, M. Krebs, S. Trattnig, and M. Krssák, "Phosphatidylcholine contributes to in vivo ^{31}P MRS signal from the human liver," *European Radiology*, vol. 25, no. 7, pp. 2059–2066, 2015.

[82] J.-L. Gallis, M.-C. Delmas-Beauvieux, M. Biran, N. Rousse, T. Durand, and P. Canioni, "Is cellular integrity responsible for the partial NMR invisibility of ATP in isolated ischemic rat liver?" *NMR in Biomedicine*, vol. 4, no. 6, pp. 279–285, 1991.

[83] S. Masson and B. Quistorff, "The phosphorous-31 NMR visibility of ATP in perfused rat liver remains about 90 %, unaffected by changes of metabolic state," *Biochemistry*, vol. 31, no. 33, pp. 7488–7493, 1992.

[84] A. Petersen, F. Kappler, B. S. Szwergold, and T. R. Brown, "Fructose metabolism in the human erythrocyte. Phosphorylation to fructose 3-phosphate," *The Biochemical Journal*, vol. 284 (Pt 2), no. Pt 2, pp. 363–366, 1992.

[85] R. F. E. Wolf, E. B. Haagsma, R. L. Kamman, E. L. Mooyaart, W. J. Sluiter, and M. J. H. Sloof, "Noninvasive metabolic assessment of human donor livers: Prognostic value of ^{31}P-magnetic resonance spectroscopy for early graft function," *Transplantation*, vol. 64, no. 1, pp. 147–152, 1997.

[86] D. Stefan, F. D. Cesare, A. Andrasescu, E. Popa, A. Lazariev, E. Vescovo, O. Strbak, S. Williams, Z. Starcuk, M. Cabanas, D. van Ormondt, and D. Graveron, "Quantitation of magnetic resonance spectroscopy signals: the jmrui software package," p. 104035, 2009.

[87] L. Vanhamme, A. van den Boogaart, and S. V. Huffel, "Improved method for accurate and efficient quantification of MRS data with use of prior knowledge," *Journal of Magnetic Resonance*, vol. 129, no. 1, pp. 35–43, 1997.

[88] A. Kotronen, M. Peltonen, A. Hakkarainen, K. Sevastianova, R. Bergholm, L. M. Johansson, N. Lundbom, A. Rissanen, M. Ridderstråle, L. Groop, M. Orho-Melander, and H. Yki-Järvinen, "Prediction of non-alcoholic fatty liver disease and liver fat using metabolic and genetic factors," *Gastroenterology*, vol. 137, no. 3, pp. 865–872, 2009.

[89] E. J. Murphy, B. Rajagopalan, K. M. Brindle, and G. K. Radda, "Phospholipid bilayer contribution to ^{31}P NMR spectra in vivo," *Magnetic Resonance in Medicine*, vol. 12, no. 2, pp. 282–289, 1989.

[90] R. Buchli, D. Meier, E. Martin, and P. Boesiger, "Assessment of absolute metabolite concentrations in human tissue by ^{31}P MRS in vivo. Part II: Muscle, liver, kidney," *Magnetic Resonance in Medicine*, vol. 32, no. 4, pp. 453–458, 1994.

[91] M. Ljungberg, G. Starck, B. Vikhoff-Baaz, M. Alpsten, S. Ekholm, and E. Forssell-Aronsson, "Extended ISIS sequences insensitive to T1 smearing," *Magnetic Resonance in Medicine*, vol. 44, no. 4, pp. 546–555, 2000.

[92] W. W. Lautt, "Hepatic vasculature: a conceptual review," *Gastroenterology*, vol. 73, no. 5, pp. 1163–1169, 1977.

[93] K. Höckerstedt, L. Aaltonen, T. Ripatti, and H. Schmidt, *Gastroenterologia*, 2nd ed. Helsinki: Duodecim, 2000.

[94] P. C. Dagnelie, J. D. Bell, I. J. Cox, D. K. Menon, J. Sargentoni, G. A. Coutts, and S. C. R. Williams, "Effects of fish oil on phospholipid metabolism in human and rat liver studied by ^{31}P NMR spectroscopy in vivo and in vitro," *NMR in Biomedicine*, vol. 6, no. 2, pp. 157–162, 1993.

[95] D. M. Small, M. Bourges, and D. G. Dervichian, "Ternary and quaternary aqueous systems containing bile salt, lecithin, and cholesterol," *Nature*, vol. 211, no. 5051, pp. 816–818, 1966.

[96] O. B. Ijare, T. Bezabeh, N. Albiin, A. Bergquist, U. Arnelo, M. Lohr, and I. C. Smith, "Potential of ^{31}P magnetic resonance spectroscopy of bile in the detection of cholestatic diseases," in *Proceedings of the International Society for Magnetic Resonance in Medicine*, vol. 19, 2011, paper 1002.

[97] M. Chmelik, M. Povazan, M. Krssák, S. Gruber, M. Tkacov, S. Trattnig, and W. Bogner, "In vivo ^{31}P magnetic resonance spectroscopy of the human liver at 7 T: an initial experience," *NMR in Biomedicine*, vol. 27, no. 4, pp. 478–485, 2014.